Gain-Scheduled $\mathcal{H}_\infty$ Loop-Shaping Autopilot Design for Spin-Stabilized Canard-Guided Projectiles

F. Sève, S. Theodoulis, P. Wernert
(French-German Research Institute of Saint-Louis (ISL), Department of Guidance Navigation and Control, Saint-Louis (FR))

M. Zasadzinski, M. Boutayeb
(Research Center for Automatic Control of Nancy (CRAN), University of Lorraine, UMR 7039, CNRS, Cosnes-et-Romain (FR))

E-mail: Florian.Seve@isl.eu

DOI: 10.12762/2017.AL13-03

This article is dedicated to the design of a complete guidance & control system for the roll/pitch/yaw-channels of a 155 mm dual-spin projectile equipped with nose-mounted trajectory correction canards. The projectile airframe parameter-dependent nonlinear model including aerodynamic and actuator/sensor uncertainty descriptions is given and the subsequently computed linearized models necessary for autopilot design are presented. The pitch/yaw-channel dynamics linearized system is useful for highlighting important properties specific to these dynamics, in particular in relation with the parameter vector dimension and the sensor position. The computation of a linear structured controller for the nose roll-axis and of a gain-scheduled structured compensator for the airframe pitch/yaw-axes, using an $\mathcal{H}_\infty$ loop-shaping design approach, is detailed with the assessment of the obtained performance and robustness properties. Finally, various guided flight nonlinear 7DoF simulation results are exposed for the purpose of evaluating over the projectile flight envelope the effectiveness of the proposed guidance & control scheme.

Introduction

Destroying a target on a battlefield with an artillery unit traditionally requires several ballistic rounds to be fired due to the lack of accuracy of such weapons. Significant ballistic impact point miss distances can originate from incorrect launch initial conditions (muzzle velocity and gun barrel pointing and azimuth) or wind perturbations. However, the multiplication of the number of firings causes potential unwanted collateral damage, pushes the mission costs higher, and can lead to an excessive engagement time and logistical issues that render the artillery crew vulnerable to enemy counter fire. The interest of industrial and academic communities in developing projectile trajectory correction mechanisms has grown over the last forty years, in order to improve the ballistic shell terminal accuracy and subsequently to overcome the aforementioned drawbacks.

An attractive approach consists in equipping a projectile with aerodynamic control surfaces, despite their fragile mechanical structure, which can be rotating or reciprocating nose-mounted canards, tail fins, or both [24, 31, 10, 26, 12, 9, 33, 13, 34]. Those possess the advantage of creating efforts that are quite easily modeled and the generated control is a continuous-time signal. In addition, these trajectory control mechanisms are very similar to the well-mastered ones mounted on traditional missiles [35, 29, 36, 3, 25, 37, 7]. The projectile concept studied here results from retrofitting an existing unguided 155 mm ballistic *spin-stabilized* shell with a roll-decoupled nose equipped with two pairs of rotating canards, hence leading to a so-called *dual-spin* control configuration. The latter is also, here, of a *Skid-To-Turn* (STT) type, *i.e.*, the projectile trajectory correction is performed thanks to maneuvers in the pitch and yaw planes using the two pairs of canards, while the nose is maintained at a fixed angular position. The previous guided spin-stabilized projectile concept, which is dynamically stabilized thanks to its high body roll rate [21, 6], is attractive for maintaining low development and production costs. However, spin-stabilization, which causes a strong coupling between the highly nonlinear pitch/yaw-channel dynamics, makes the design of a truly multivariable nose-embedded guidance & control (G&C) function necessary in order to devise a smart weapon, which is more challenging than for classical missiles with decoupled pitch and yaw axes.

The flight G&C system, which must retain a quite simple structure, easy to tune and implement while delivering high-performance over a large operating domain, has to handle additional constraints, such as

the use of low-cost, small and gun-hardened actuators and sensors with limited performance, which are also inevitably integrated in the projectile nose and not at the center of mass (CM), as is usually done in the literature regarding guided projectiles. Considering this severe practical position restriction constitutes a major novelty with respect to the previous works of [33, 34]. In addition, sensor measurement noise and aerodynamic and component uncertainty, along with external disturbances, must be taken into account.

The linearization-based divide-and-conquer gain-scheduling control approach [19, 27] coupled with the linear robust control theory tools [41, 30] have proven their value in computing efficient autopilots for aerospace applications. Hence, the parameter-dependent nonlinear system dynamics are first linearized around an equilibrium manifold covering the operating domain [20]. The set of designed linear controllers is then smoothly interpolated to yield a gain-scheduled controller, in order to operate at any nonlinear system operating point. However, the previous local control design technique lacks global stability and performance property guarantee, hence necessitating a multitude of nonlinear simulations to be performed for validation. With regard to the design of guidance module, proportional navigation (PN) algorithms are traditionally used in the case of missiles.

This paper is aimed at extending and improving the works of [33, 34] concerning autopilot design for guided ammunition. A nonlinear model for the complete projectile dynamics is first presented, based on a more generic aerodynamic force and moment description, in addition to the aforementioned critical sensor position constraint. Distinct linearized models for the nose roll and for the complete projectile pitch/yaw dynamics are then computed to design, using an $\mathcal{H}_\infty$ loop-shaping design procedure [22, 23] offering an alternative to the standard robust control technique used in [34], separate two-degree-of-freedom (2DoF) fixed structure and reduced order autopilots. Indeed, the regulated roll-channel dynamics must respond faster than the controlled pitch/yaw ones in the STT control configuration employed.

A single robust linear controller is sufficient for the purpose of controlling the nose roll-channel throughout the projectile flight envelope, whereas a gain-scheduling control strategy is developed for the parameter-highly varying pitch/yaw dynamics. A robust stability analysis is then proposed for both linear controller designs using various robustness tools, such as μ-analysis [41, 30]. Finally, the effectiveness of the obtained PN guidance & gain-scheduled control system to intercept a ballistic impact point is assessed through extensive nonlinear simulations.

This paper is organized as follows. The first part addresses the development of the projectile nonlinear and linearized models. The second part presents the autopilot designs and robustness analyses for both the nose roll-channel and the complete projectile pitch/yaw-channels. The third part addresses PN guidance. Finally, the fourth part details nonlinear simulation results for the STT guided projectile.

Airframe Modeling

Canard-Guided Projectile Concept

The studied dual-spin STT canard-guided projectile concept is given in Fig. 1 with several of the flight mechanics state and control variables used in the nonlinear mathematical model representing its behavior. The rapidly spinning aft part incorporates the explosive charge, whereas the forward part embeds two servomotors deflecting the steering canards and a coaxial servomotor used for decoupling and controlling the nose roll-axis dynamics. The forward part also integrates a three-axis IMU assisted by a GPS module, along with the necessary guidance and control processors.

Nonlinear Parameter-Dependent Dynamics & Kinematics

The 7DoF nonlinear model for a canard-guided dual-spin projectile is composed of translational & attitude *dynamic* equations. The first ones describe the linear motion of the projectile CM B with respect to the Earth inertial frame E, whereas the second ones represent the rotational movements of the forward "f" and aft "a" projectile parts $\mathrm{B_f}$, $\mathrm{B_a}$ with respect to the inertial frame. Those dynamic equations, which are expressed in a coordinate system (CS) related to a non-rolling frame $\mathrm{B'}$, are defined as:

$$\begin{bmatrix} \dot{u} \\ \dot{v} \\ \dot{w} \end{bmatrix} = \left(\frac{1}{m}\right)\begin{bmatrix} X \\ Y \\ Z \end{bmatrix} - \begin{bmatrix} 0 & -r & q \\ r & 0 & r\tan\theta \\ -q & -r\tan\theta & 0 \end{bmatrix}\begin{bmatrix} u \\ v \\ w \end{bmatrix} \tag{1a}$$

$$\begin{bmatrix} \dot{p}_\mathrm{f} \\ \dot{p}_\mathrm{a} \\ \dot{q} \\ \dot{r} \end{bmatrix} = \begin{bmatrix} 0 \\ 0 \\ -\left(I_{\mathrm{xa}} I_\mathrm{t}^{-1} p_\mathrm{a} + r\tan\theta\right) r \\ \left(I_{\mathrm{xa}} I_\mathrm{t}^{-1} p_\mathrm{a} + r\tan\theta\right) q \end{bmatrix} + \left[\begin{array}{c|ccc} I_{\mathrm{xf}}^{-1} & 0 & 0 & 0 \\ \hline 0 & I_{\mathrm{xa}}^{-1} & 0 & 0 \\ 0 & 0 & I_\mathrm{t}^{-1} & 0 \\ 0 & 0 & 0 & I_\mathrm{t}^{-1} \end{array}\right]\begin{bmatrix} L_\mathrm{f} \\ L_\mathrm{a} \\ M \\ N \end{bmatrix} \tag{1b}$$

The nonlinear model comprises additional translational & attitude *kinematic* equations symbolizing a change from the inertial CS to the non-rolling frame CS that is applied to the linear and angular velocities of both projectile parts:

$$\begin{bmatrix} \dot{x}_\mathrm{e} \\ \dot{y}_\mathrm{e} \\ \dot{z}_\mathrm{e} \end{bmatrix} = \begin{bmatrix} \cos\psi\cos\theta & -\sin\psi & \cos\psi\sin\theta \\ \sin\psi\cos\theta & \cos\psi & \sin\psi\sin\theta \\ -\sin\theta & 0 & \cos\theta \end{bmatrix}\begin{bmatrix} u \\ v \\ w \end{bmatrix} \tag{2a}$$

$$\begin{bmatrix} \dot{\phi}_\mathrm{f} \\ \dot{\phi}_\mathrm{a} \\ \dot{\theta} \\ \dot{\psi} \end{bmatrix} = \begin{bmatrix} 1 & 0 & 0 & \tan\theta \\ 0 & 1 & 0 & \tan\theta \\ 0 & 0 & 1 & 0 \\ 0 & 0 & 0 & \sec\theta \end{bmatrix}\begin{bmatrix} p_\mathrm{f} \\ p_\mathrm{a} \\ q \\ r \end{bmatrix} \tag{2b}$$

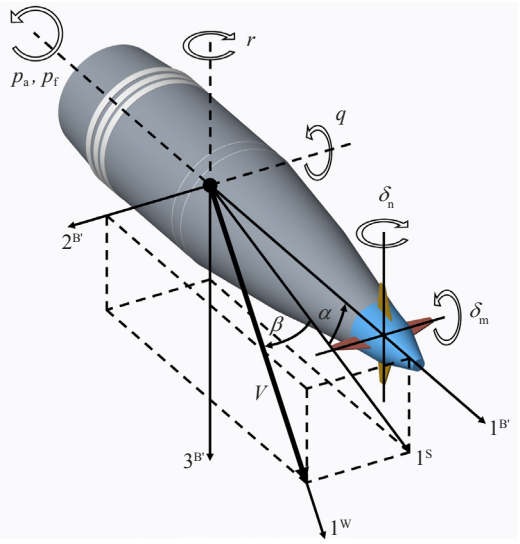

Figure 1 – 155 mm canard-guided dual-spin projectile concept

The system dynamic state variables in Eqs. (1), (2) are the projectile CM linear $[u\ \ v\ \ w]^{\mathrm{T}} = [\boldsymbol{v}_{\mathrm{B}}^{\mathrm{E}}]^{\mathrm{B}'}$ velocities and the forward and aft part angular $[p_{\mathrm{f}}\ \ p_{\mathrm{a}}\ \ q\ \ r]^{\mathrm{T}} = [\boldsymbol{\omega}^{\mathrm{B_{fa}E}}]^{\mathrm{B}'}$ rates. The system kinematic states are the CM linear $[x_{\mathrm{e}}\ \ y_{\mathrm{e}}\ \ z_{\mathrm{e}}]^{\mathrm{T}} = [\boldsymbol{s}_{\mathrm{BE}}]^{\mathrm{E}}$ positions and the body and nose angular $[\phi_{\mathrm{f}}\ \ \phi_{\mathrm{a}}\ \ \theta\ \ \psi]^{\mathrm{T}} = \boldsymbol{e}^{\mathrm{B_{fa}E}}$ orientations. The external forces X, Y, Z are composed of gravitational (g) and aerodynamic contributions [drag/lift forces being mainly applied to the projectile body (dl), canards (c) and Magnus (m)] and are given by:

$$\begin{bmatrix} X \\ Y \\ Z \end{bmatrix} = \begin{bmatrix} X_{\mathrm{dl}} \\ Y_{\mathrm{dl}} \\ Z_{\mathrm{dl}} \end{bmatrix} + \begin{bmatrix} X_{\mathrm{c}} \\ Y_{\mathrm{c}} \\ Z_{\mathrm{c}} \end{bmatrix} + \begin{bmatrix} X_{\mathrm{m}} \\ Y_{\mathrm{m}} \\ Z_{\mathrm{m}} \end{bmatrix} + \begin{bmatrix} X_{\mathrm{g}} \\ Y_{\mathrm{g}} \\ Z_{\mathrm{g}} \end{bmatrix}$$
$$= \bar{q}S \left(\begin{bmatrix} -C_{\mathrm{A0}}(\mathcal{M},\alpha,\beta) \\ C_{\mathrm{Y0}}(\mathcal{M},\beta) \\ -C_{\mathrm{N0}}(\mathcal{M},\alpha) \end{bmatrix} + \begin{bmatrix} 0 \\ C_{\mathrm{Y}\delta}(\mathcal{M})(\delta_{\mathrm{z}} - \beta) \\ -C_{\mathrm{N}\delta}(\mathcal{M})(\delta_{\mathrm{y}} + \alpha) \end{bmatrix} \right. \tag{3}$$
$$\left. + \left(\frac{p_{\mathrm{a}} d}{V}\right) \begin{bmatrix} 0 \\ C_{\mathrm{Y}p}(\mathcal{M},\alpha,\beta) \\ -C_{\mathrm{N}p}(\mathcal{M},\alpha,\beta) \end{bmatrix} \right) + mg \begin{bmatrix} -\sin\theta \\ 0 \\ \cos\theta \end{bmatrix}$$

The external moments consist of similar aerodynamic components, along with additional aerodynamic damping (d) and mechanical control/friction (cf) terms:

$$\begin{bmatrix} L_{\mathrm{f}} \\ L_{\mathrm{a}} \\ M \\ N \end{bmatrix} = \begin{bmatrix} L_{\mathrm{f,dl}} \\ L_{\mathrm{a,dl}} \\ M_{\mathrm{dl}} \\ N_{\mathrm{dl}} \end{bmatrix} + \begin{bmatrix} L_{\mathrm{f,c}} \\ L_{\mathrm{a,c}} \\ M_{\mathrm{c}} \\ N_{\mathrm{c}} \end{bmatrix} + \begin{bmatrix} L_{\mathrm{f,m}} \\ L_{\mathrm{a,m}} \\ M_{\mathrm{m}} \\ N_{\mathrm{m}} \end{bmatrix} + \begin{bmatrix} L_{\mathrm{f,d}} \\ L_{\mathrm{a,d}} \\ M_{\mathrm{d}} \\ N_{\mathrm{d}} \end{bmatrix} + \begin{bmatrix} L_{\mathrm{f,cf}} \\ L_{\mathrm{a,cf}} \\ M_{\mathrm{cf}} \\ N_{\mathrm{cf}} \end{bmatrix}$$
$$= \bar{q}Sd \left(\begin{bmatrix} 0 \\ 0 \\ C_{\mathrm{m0}}(\mathcal{M},\alpha) \\ C_{\mathrm{n0}}(\mathcal{M},\beta) \end{bmatrix} + \begin{bmatrix} 0 \\ 0 \\ C_{\mathrm{m}\delta}(\mathcal{M})(\delta_{\mathrm{z}} + \alpha) \\ C_{\mathrm{n}\delta}(\mathcal{M})(\delta_{\mathrm{y}} - \beta) \end{bmatrix} \right. \tag{4}$$
$$\left. + \left(\frac{p_{\mathrm{a}} d}{V}\right) \begin{bmatrix} 0 \\ 0 \\ C_{\mathrm{m}p}(\mathcal{M},\alpha,\beta) \\ C_{\mathrm{n}p}(\mathcal{M},\alpha,\beta) \end{bmatrix} + \left(\frac{d}{V}\right) \begin{bmatrix} 0 \\ C_{lp}(\mathcal{M}) p_{\mathrm{a}} \\ C_{mq}(\mathcal{M}) q \\ C_{nr}(\mathcal{M}) r \end{bmatrix} \right) + \begin{bmatrix} L_{\mathrm{co}} + L_{\mathrm{f-a}} \\ -L_{\mathrm{f-a}} \\ 0 \\ 0 \end{bmatrix}$$

The coaxial motor torque is denoted by L_{co}, whereas the friction moment $L_{\mathrm{f-a}}$ created between the forward and aft parts is defined as:

$$L_{\mathrm{f-a}} = \bar{q}Sd\, C_{\mathrm{A0}}(\mathcal{M},\alpha,\beta_{\mathrm{F}}) \cdot \mathrm{sign}(p_{\mathrm{a}} - p_{\mathrm{f}}) \left(K_{\mathrm{s}} + K_{\mathrm{v}} |p_{\mathrm{a}} - p_{\mathrm{f}}|\right) \tag{5}$$

The variables $\delta_{\mathrm{z}}, \delta_{\mathrm{y}}$ are the system virtual normal and lateral control signals, which depend on the actual canard pair deflections $\delta_{\mathrm{m}}, \delta_{\mathrm{n}}$ and on the nose roll angular position ϕ_{f} as:

$$\begin{bmatrix} \delta_{\mathrm{z}} \\ \delta_{\mathrm{y}} \end{bmatrix} = \begin{bmatrix} \cos\phi_{\mathrm{f}} & -\sin\phi_{\mathrm{f}} \\ \sin\phi_{\mathrm{f}} & \cos\phi_{\mathrm{f}} \end{bmatrix} \begin{bmatrix} \delta_{\mathrm{m}} \\ \delta_{\mathrm{n}} \end{bmatrix} = \mathbf{T}(\phi_{\mathrm{f}}) \begin{bmatrix} \delta_{\mathrm{m}} \\ \delta_{\mathrm{n}} \end{bmatrix} \tag{6}$$

The elements $C_{\mathrm{A0}}, C_{\mathrm{Y0}}, C_{\mathrm{N0}}$ represent the drag/lift-induced, $C_{\mathrm{Y}\delta}, C_{\mathrm{N}\delta}$ the canard, and $C_{\mathrm{Y}p}, C_{\mathrm{N}p}$ the Magnus force aerodynamic coefficients, whereas the elements $C_{\mathrm{m0}}, C_{\mathrm{n0}}$ symbolize the drag/lift-induced, $C_{\mathrm{m}\delta}, C_{\mathrm{n}\delta}$ the canard, $C_{\mathrm{m}p}, C_{\mathrm{n}p}$ the Magnus, and C_{lp}, C_{mq}, C_{nr} the damping moment aerodynamic coefficients. Due to imperfect wind-tunnel measurements and computational fluid dynamics simulation results, those aerodynamic coefficients (and their partial derivatives used below in the linearized model) take uncertain values with variations around the nominal values of up to 5% for C_{A0}, 10% for $C_{\mathrm{Y0}}, C_{\mathrm{N0}}, C_{\mathrm{m0}}, C_{\mathrm{n0}}, C_{\mathrm{Y}\delta}, C_{\mathrm{N}\delta}$ and $C_{\mathrm{m}\delta}, C_{\mathrm{n}\delta}$, 20% for C_{lp}, and 30% for $C_{\mathrm{Y}p}, C_{\mathrm{N}p}, C_{\mathrm{m}p}, C_{\mathrm{n}p}$ and C_{mq}, C_{nr}. All of the aerodynamic coefficients are tabulated in a highly nonlinear manner as a function of the Mach number $\mathcal{M} = V/a$, and of the aerodynamic angles of attack (AoA) α and sideslip (AoS) β for some of them. The airframe velocity V and the angles α, β given in Fig. 1 are defined as follows under a no-wind assumption [40]:

$$V = \sqrt{u^2 + v^2 + w^2} \tag{7a}$$

$$\alpha = \arctan\left(\frac{w}{u}\right) \tag{7b}$$

$$\beta = \arcsin\left(\frac{v}{V}\right) = \arctan\left(\frac{v}{\sqrt{u^2 + w^2}}\right) \tag{7c}$$

The preceding force and moment dynamic equations (1) also depend on the altitude-dependent $(h = |z_{\mathrm{e}}|)$ gravitational acceleration $g(h)$, on the projectile mass m and on the roll-axis projectile forward and aft part moments of inertia $I_{\mathrm{xf}}, I_{\mathrm{xa}}$, along with the transversal moment of inertia I_{t}. Finally, the forces and moments (3)-(5) are parameterized by the reference area S, caliber d, and static and viscous friction coefficients $K_{\mathrm{s}}, K_{\mathrm{v}}$, and they vary with the dynamic pressure $\bar{q} = \frac{1}{2}\rho V^2$, where $\rho = \rho(h)$ and $a = a(h)$ are the altitude-dependent air density and speed of sound.

As is generally done in the literature [8, 5], the complete aforementioned translational nonlinear dynamic equations include the linear velocities (u, v, w) as state variables, which are however less suited for pitch/yaw-channel autopilot design than the wind-frame W variables (V, α, β). Equivalent (under a no-wind assumption) nonlinear translational dynamic equations using the states (V, α, β) are hence preferred, and those are obtained by first differentiating Eqs. (7) with respect to time:

$$\dot{V} = \frac{u\dot{u} + v\dot{v} + w\dot{w}}{V} \tag{8.a}$$

$$\dot{\alpha} = \frac{u\dot{w} - w\dot{u}}{u^2 + w^2} \tag{8.b}$$

$$\dot{\beta} = \frac{-uv\dot{u} + (u^2 + w^2)\dot{v} - vw\dot{w}}{V^2\sqrt{u^2 + w^2}} \tag{8.c}$$

The projectile linear velocities, which are obtained as follows by inverting Eqs. (7):

$$u = V\cos\alpha\cos\beta \tag{9.a}$$

$$v = V\sin\beta \tag{9.b}$$

$$w = V\sin\alpha\cos\beta \tag{9.c}$$

are then inserted into the wind-frame variable dynamics equations (8) along with the expressions of $(\dot{u},\dot{v},\dot{w})$ given in Eq. (1a), in order to provide the equivalent nonlinear translational state dynamics:

$$\begin{bmatrix}\dot{V}\\ \dot{\alpha}\\ \dot{\beta}\end{bmatrix}=\begin{bmatrix}0\\ q+r\left(\cos\alpha\tan\theta-\sin\alpha\right)\tan\beta\\ -r\left(\cos\alpha+\sin\alpha\tan\theta\right)\end{bmatrix}+\left(\frac{1}{mV}\right)\begin{bmatrix}V\cos\alpha\cos\beta & V\sin\beta & V\sin\alpha\cos\beta\\ -\sin\alpha/\cos\beta & 0 & \cos\alpha/\cos\beta\\ -\cos\alpha\sin\beta & \cos\beta & -\sin\alpha\sin\beta\end{bmatrix}\begin{bmatrix}X\\ Y\\ Z\end{bmatrix} \tag{10}$$

Equivalent nonlinear translational kinematics can be derived by inserting Eqs. (9) into Eq. (2a).

The projectile nonlinear state dynamics & kinematics mathematical model in (V,α,β) is then complemented with nonlinear output dynamics & kinematics equations providing the signals measured at a longitudinal distance $x_{\text{IMU}}>0$ from the projectile CM. The output Euler angles are directly the nose state angular positions $[\phi_{\text{f}}\ \ \theta\ \ \psi]^{\text{T}}=\boldsymbol{e}^{\text{B}_{\text{f}}\text{E}}$, whereas the load factors $[n_{\text{x,f}}\ \ n_{\text{y,f}}\ \ n_{\text{z,f}}]^{\text{T}}=[\boldsymbol{n}^{\text{B}_{\text{f}}\text{E}}]^{\text{B}_{\text{f}}}$ and the angular rates $[p_{\text{f,f}}\ \ q_{\text{f}}\ \ r_{\text{f}}]^{\text{T}}=[\boldsymbol{\omega}^{\text{B}_{\text{f}}\text{E}}]^{\text{B}_{\text{f}}}$, which are obtained in the nose frame B_{f} CS from the accelerometer and gyrometer measurements, respectively, are given as follows, together with the nose GPS inertial positions $[x_{\text{f}}\ \ y_{\text{f}}\ \ z_{\text{f}}]^{\text{T}}=[\boldsymbol{s}_{\text{B}_{\text{f}}\text{E}}]^{\text{E}}$:

$$\begin{bmatrix}n_{\text{x,f}}\\ n_{\text{y,f}}\\ n_{\text{z,f}}\end{bmatrix}=\begin{bmatrix}1 & 0 & 0\\ 0 & \cos\phi_{\text{f}} & \sin\phi_{\text{f}}\\ 0 & -\sin\phi_{\text{f}} & \cos\phi_{\text{f}}\end{bmatrix}\left\{\begin{bmatrix}n_{\text{CM,x}}\\ n_{\text{CM,y}}\\ n_{\text{CM,z}}\end{bmatrix}+\left(\frac{x_{\text{IMU}}}{g}\right)\begin{bmatrix}-\left(q^2+r^2\right)\\ p_{\text{f}}q+\dot{r}\\ p_{\text{f}}r-\dot{q}\end{bmatrix}\right\} \tag{11a}$$

$$\begin{bmatrix}p_{\text{f,f}}\\ q_{\text{f}}\\ r_{\text{f}}\end{bmatrix}=\begin{bmatrix}1 & 0 & 0\\ 0 & \cos\phi_{\text{f}} & \sin\phi_{\text{f}}\\ 0 & -\sin\phi_{\text{f}} & \cos\phi_{\text{f}}\end{bmatrix}\begin{bmatrix}p_{\text{f}}\\ q\\ r\end{bmatrix} \tag{11b}$$

$$\begin{bmatrix}x_{\text{f}}\\ y_{\text{f}}\\ z_{\text{f}}\end{bmatrix}=\begin{bmatrix}x_{\text{e}}\\ y_{\text{e}}\\ z_{\text{e}}\end{bmatrix}+x_{\text{IMU}}\begin{bmatrix}\cos\psi\cos\theta\\ \sin\psi\cos\theta\\ -\sin\theta\end{bmatrix} \tag{11c}$$

where the load factors $[n_{\text{CM,x}}\ \ n_{\text{CM,y}}\ \ n_{\text{CM,z}}]^{\text{T}}=[\boldsymbol{n}^{\text{BE}}]^{\text{B}'}$ at the projectile CM and expressed in the non-rolling frame CS are equal to the specific forces divided by the projectile weight.

Linearized Dynamics

Roll-Channel

The nose roll angular position and velocity state dynamics given in Eqs. (1b), (2b) are first augmented with the coaxial DC servomotor current i linear dynamics, and the result is rearranged into the following linear parameter-dependent form:

$$\mathcal{S}_{\text{R}}^{\lambda}(\boldsymbol{\lambda}_{\text{R}}):\ \begin{bmatrix}\dot{\phi}_{\text{f}}\\ \dot{p}_{\text{f}}\\ \dot{i}\end{bmatrix}=\begin{bmatrix}0 & 1 & 0\\ 0 & -K_{\text{a}}(\boldsymbol{\lambda}_{\text{R}})K_{\text{v}} & I_{\text{xf}}^{-1}K_{\text{m}}\\ 0 & -K_{\text{b}}L^{-1} & -RL^{-1}\end{bmatrix}\begin{bmatrix}\phi_{\text{f}}\\ p_{\text{f}}\\ i\end{bmatrix}+\begin{bmatrix}d_{\phi}\\ d_{p}\\ d_{i}\end{bmatrix}+\begin{bmatrix}0\\ 0\\ L^{-1}\end{bmatrix}V_{\text{e}},\quad \boldsymbol{\lambda}_{\text{R}}\in\boldsymbol{\Gamma}_{\text{R}}^{\lambda} \tag{12}$$

with:

$$K_{\text{a}}(\boldsymbol{\lambda}_{\text{R}})=\left(\frac{\bar{q}Sd}{I_{\text{xf}}}\right)C_{\text{A0}}(\mathcal{M},\alpha,\beta) \tag{13}$$

and the time-varying parameter vector $\boldsymbol{\lambda}_{\text{R}}=[V\ \ \alpha\ \ \beta\ \ h]^{\text{T}}$ capturing the dependence of the system dynamics on the projectile operating condition, and taking its values inside an operating domain $\boldsymbol{\Gamma}_{\text{R}}^{\lambda}\subset\mathbb{R}^4$. The system inputs are the control applied voltage V_{e} with a saturation level $V_{\text{e,sat}}=\pm 60\ \text{V}$ and the time-varying external disturbances d_{ϕ},d_{p},d_{i} defined as:

$$\boldsymbol{d}=\begin{bmatrix}d_{\phi}\\ d_{p}\\ d_{i}\end{bmatrix}=\begin{bmatrix}r\tan\theta\\ K_{\text{a}}(\boldsymbol{\lambda}_{\text{R}})\left[\text{sign}\left(p_{\text{a}}-p_{\text{f}}\right)K_{\text{s}}+K_{\text{v}}p_{\text{a}}\right]\\ K_{\text{b}}L^{-1}p_{\text{a}}\end{bmatrix} \tag{14}$$

The electromotive force constant K_{b}, the motor inductance L, resistance R, and torque constant K_{m} verifying $L_{\text{co}}=K_{\text{m}}i$, along with the viscous friction coefficient K_{v} are taken as real uncertain parameters with errors of 15% for $L,R,K_{\text{b}},K_{\text{m}}$ and of 40% for K_{v}.

Finally, the projectile flight-condition dependence of the model $\mathcal{S}_{\text{R}}^{\lambda}(\boldsymbol{\lambda}_{\text{R}})$ is transformed into an uncertainty on the aerodynamic element $K_{\text{a}}(\boldsymbol{\lambda}_{\text{R}})$ corresponding to its variations over $\boldsymbol{\Gamma}_{\text{R}}^{\lambda}$, and to the errors on the axial force aerodynamic coefficient C_{A0}. This practice leads to defining a new unique uncertain linear (not parameter-dependent) model $\Sigma_{\text{R}}^{\lambda}$ used for nose roll-channel autopilot design, with the nose angular position and rate being the feedback signals.

Pitch/Yaw-Channels

The STT projectile trajectory correction feedback system, which acts on the nonlinear pitch/yaw axis dynamics represented by the α,q and β,r state dynamic equations in Eqs. (10), (1b), uses the canard deflections $\boldsymbol{\delta}=[\delta_{\text{m}}\ \ \delta_{\text{n}}]^{\text{T}}$ as the control inputs, the normal/lateral load factors $\boldsymbol{n}_{\text{zy,f}}=[n_{\text{z,f}}\ \ n_{\text{y,f}}]^{\text{T}}$ as the tracking outputs, and the pitch/yaw angular rates $\boldsymbol{\omega}_{qr,\text{f}}=[q_{\text{f}}\ \ r_{\text{f}}]^{\text{T}}$ as additional measured outputs. The state and output pitch/yaw dynamics are directly influenced by the airframe airspeed V, the projectile nose and body rates $p_{\text{f}},p_{\text{a}}$ and some of the kinematic states. Actually, the normal inertial position z_{e} enters the aerodynamic coefficient and dynamic pressure expressions, the pitch angle θ influence is due to the flight mechanics equation structure, and the nose roll angle ϕ_{f} is used in the virtual control and measured output expressions. A parameter vector $\boldsymbol{\sigma}_{\text{PY}}=[V\ \ p_{\text{f}}\ \ p_{\text{a}}\ \ h\ \ \phi_{\text{f}}\ \ \theta]^{\text{T}}$ is then defined, takes its values from a set $\boldsymbol{\Gamma}_{\text{PY}}^{\sigma}\subset\mathbb{R}^6$ and is considered as a relatively slowly-varying external input to the pitch/yaw dynamics.

In the context of a linearization-based, divide-and-conquer gain-scheduling control strategy, the computation of a pitch/yaw dynamics linearized model needs to calculate a set of equilibrium points for any admissible fixed value of the parameter vector $\boldsymbol{\sigma}_{\text{PY}}$ by imposing $\dot{\alpha}=\dot{\beta}=\dot{q}=\dot{r}=0$. The result is an underdetermined system of four nonlinear algebraic equations with the six unknown states α,β,q,r and controls $\delta_{\text{m}},\delta_{\text{n}}$. A solution for making the problem solvable is to define an *extended* trimming vector $\boldsymbol{\rho}_{\text{PY}}=[V\ \alpha\ \beta\ p_{\text{f}}\ \ p_{\text{a}}\ h\ \phi_{\text{f}}\ \theta]^{\text{T}}\in\boldsymbol{\Gamma}_{\text{PY}}^{\rho}\subset\mathbb{R}^8$ by imposing the aerodynamic angles α,β. An efficient home-made trimming analytical procedure that is specifically developed for spin-stabilized projectiles with strongly coupled pitch/yaw-axes dynamics can be found in [33].

The linearized model, whose state-space matrix elements are functions of the trimming vector $\boldsymbol{\rho}_{\mathrm{PY}}$, and which possesses a q-LPV form due to the trimming vector dependence on the system states α, β, is expressed in the following generic form:

$$\mathcal{S}^{\rho}_{\mathrm{PY}}\left(\boldsymbol{\rho}_{\mathrm{PY}}\right): \left[\begin{array}{c} \dot{\boldsymbol{x}}_{\mathrm{PY},\varepsilon}(t) \\ \boldsymbol{y}_{\mathrm{PY},\varepsilon}(t) \end{array}\right] = \left[\begin{array}{c|c} \mathbf{A}\left(\boldsymbol{\rho}_{\mathrm{PY}}\right) & \mathbf{B}\left(\boldsymbol{\rho}_{\mathrm{PY}}\right) \\ \hline \mathbf{C}\left(\boldsymbol{\rho}_{\mathrm{PY}}\right) & \mathbf{D}\left(\boldsymbol{\rho}_{\mathrm{PY}}\right) \end{array}\right] \left[\begin{array}{c} \boldsymbol{x}_{\mathrm{PY},\varepsilon}(t) \\ \boldsymbol{u}_{\mathrm{PY},\varepsilon}(t) \end{array}\right], \quad \forall \boldsymbol{\rho}_{\mathrm{PY}} \in \boldsymbol{\Gamma}^{\rho}_{\mathrm{PY}},\ t \in \mathbb{R}^{+} \tag{15}$$

with the state $\boldsymbol{x}_{\mathrm{PY},\varepsilon}(t) = \boldsymbol{x}_{\mathrm{PY}}(t) - \boldsymbol{x}_{\mathrm{PY}}[\boldsymbol{\rho}_{\mathrm{PY}}(t)] = [\alpha_{\varepsilon}\ q_{\varepsilon}\ \beta_{\varepsilon}\ r_{\varepsilon}]^{\mathrm{T}}$, the control $\boldsymbol{u}_{\mathrm{PY},\varepsilon}(t) = \boldsymbol{u}_{\mathrm{PY}}(t) - \boldsymbol{u}_{\mathrm{PY}}[\boldsymbol{\rho}_{\mathrm{PY}}(t)] = [\delta_{\mathrm{m},\varepsilon}\ \delta_{\mathrm{n}_z\varepsilon}]^{\mathrm{T}}$ and the output $\boldsymbol{y}_{\mathrm{PY},\varepsilon}(t) = \boldsymbol{y}_{\mathrm{PY}}(t) - \boldsymbol{y}_{\mathrm{PY}}[\boldsymbol{\rho}_{\mathrm{PY}}(t)] = [n_{z,\varepsilon}\ n_{y,\varepsilon}\ q_{\varepsilon}\ r_{\varepsilon}]^{\mathrm{T}}$ deviation vectors. The state-space matrices $\mathbf{A}(\boldsymbol{\rho}_{\mathrm{PY}})$, $\mathbf{B}(\boldsymbol{\rho}_{\mathrm{PY}})$, $\mathbf{C}(\boldsymbol{\rho}_{\mathrm{PY}})$ and $\mathbf{D}(\boldsymbol{\rho}_{\mathrm{PY}})$ are given below by Eqs. (16a)-(16d), in which the matrix $\overline{\mathbf{T}}(\phi_{\mathrm{f}})$ is the transpose of $\mathbf{T}(\phi_{\mathrm{f}})$ defined in Eq. (6). Similar expressions for the force $Z_{\alpha\alpha}, Z_{\alpha\beta}, Z_{\beta\alpha}, Z_{\beta\beta}$ and the moment $M_{q\alpha}, M_{qq}, M_{q\beta}, M_{qr}, M_{q\delta_z}$, $M_{r\alpha}, M_{rq}, M_{r\beta}, M_{rr}, M_{r\delta_y}$ elements of Eqs. (16a)-(16d) and for the load factor elements $N_{n_z\alpha}, N_{n_z\beta}, N_{n_y\alpha}, N_{n_y\beta}, N_{n_z\delta_z}, N_{n_y\delta_y}$ of Eqs. (16c), (16d) can be found in detail in [34].

As shown in [33], the stability matrix of the q-LPV model given in Eq. (16a) is very useful for highlighting the important pitch/yaw-axes dynamics cross-coupling of spin-stabilized projectiles, which is caused by their high body roll rate p_{a}. Hence, the design of a separate autopilot for each axis, as for missiles, is to be undoubtedly avoided since the resulting closed-loop system would experience poor performance and even instability.

The pitch/yaw-dynamics q-LPV model finds also four important applications in addition to autopilot design, which are only summarized here for brevity. The first application concerns a pitch/yaw-axis internal dynamics analysis [33], from which the two precession and nutation modes that are specific to spin-stabilized bodies as stated by the classical aeroballistic theory [6, 21], are clearly identified. The second application addresses the investigation of open-loop local stability properties and shows that a spin-stabilized projectile, which should be unstable statically by referring to non-spinning missile stability theory [36, 16], is however maintained stable dynamically thanks to the sufficiently high body roll rate [33].

The third application demonstrates, through a sensitivity analysis, that retaining only the airframe airspeed and altitude in a reduced dimension, slowly-varying and fully-measurable trimming vector $\boldsymbol{\lambda}_{\mathrm{PY}} = [V\ \ h]^{\mathrm{T}} \in \boldsymbol{\Gamma}^{\lambda}_{\mathrm{PY}} \subset \boldsymbol{\Gamma}^{\rho}_{\mathrm{PY}}$ is sufficient to maintain a good local approximation of the nonlinear dynamics with a resulting simplified q-LPV model $\mathcal{S}^{\lambda}_{\mathrm{PY}}(\boldsymbol{\lambda}_{\mathrm{PY}})$ parameterized by $\boldsymbol{\lambda}_{\mathrm{PY}}$. This practice leads to significantly attenuating the computational burden, thanks to a reduction in the number of controllers to be designed now for a trimming envelope $\boldsymbol{\Gamma}^{\lambda}_{\mathrm{PY}}$ of a dimension of 2 only, instead of 8 initially. In addition, the gain-scheduling control design method is more easily adapted for any value of the reduced two-dimension trimming vector, and the complexity of the implemented controller interpolation law is reduced. However, this practice introduces additional uncertainty on the trimming operating point, making the design of an autopilot even more challenging.

Finally, the fourth application shows the influence of the accelerometer position on the pitch/yaw load factor output nonlinear dynamics, and the necessity of considering the actual position for designing the best possible autopilot [28]. The actual position of the nose-embedded accelerometers is critical and needs a specific treatment due to low-frequency non-minimum phase (NMP) transmission zeros in the I/O SISO load factor-related transfer functions of the linearized model, which are close to the autopilot desired bandwidth [2, 15].

The projectile simplified q-LPV model $\mathcal{S}^{\lambda}_{\mathrm{PY}}(\boldsymbol{\lambda}_{\mathrm{PY}})$ is now augmented for autopilot design by uncertain 2nd order linear models for the canard

$$\mathbf{A} = \left[\begin{array}{cc|cc} Z_{\alpha\alpha} & 1 & Z_{\alpha\beta} & \tan\beta(\cos\alpha\tan\theta - \sin\alpha) \\ M_{q\alpha} & M_{qq} & M_{q\beta} & M_{qr} \\ \hline Z_{\beta\alpha} & 0 & Z_{\beta\beta} & -(\sin\alpha\tan\theta + \cos\alpha) \\ M_{r\alpha} & M_{rq} & M_{r\beta} & M_{rr} \end{array}\right] \tag{16a}$$

$$\mathbf{B} = \left[\begin{array}{c|c} -\left(\dfrac{\bar{q}S}{mV}\right)\left(\dfrac{\cos\alpha}{\cos\beta}\right)C_{\mathrm{N}\delta} & 0 \\ M_{q\delta_z} & 0 \\ \hline \left(\dfrac{\bar{q}S}{mV}\right)\sin\alpha\sin\beta\ C_{\mathrm{N}\delta} & \left(\dfrac{\bar{q}S}{mV}\right)\cos\beta\ C_{\mathrm{Y}\delta} \\ 0 & M_{r\delta_y} \end{array}\right] \cdot \mathbf{T}(\phi_{\mathrm{f}}) \tag{16b}$$

$$\mathbf{C} = \left[\overline{\mathbf{T}}(\phi_{\mathrm{f}}) \middle| \mathbb{O}_2\right] \cdot \left[\begin{array}{cc|cc} N_{n_z\alpha} - \left(\dfrac{x_{\mathrm{IMU}}}{g}\right)M_{q\alpha} & -\left(\dfrac{x_{\mathrm{IMU}}}{g}\right)M_{qq} & N_{n_z\beta} - \left(\dfrac{x_{\mathrm{IMU}}}{g}\right)M_{q\beta} & \left(\dfrac{x_{\mathrm{IMU}}}{g}\right)(p_{\mathrm{f}} - M_{qr}) \\ N_{n_y\alpha} + \left(\dfrac{x_{\mathrm{IMU}}}{g}\right)M_{r\alpha} & \left(\dfrac{x_{\mathrm{IMU}}}{g}\right)(p_{\mathrm{f}} + M_{rq}) & N_{n_y\beta} + \left(\dfrac{x_{\mathrm{IMU}}}{g}\right)M_{r\beta} & \left(\dfrac{x_{\mathrm{IMU}}}{g}\right)M_{rr} \end{array}\right] \tag{16c}$$

$$\mathbf{D} = \left[\overline{\mathbf{T}}(\phi_{\mathrm{f}}) \middle| \mathbb{O}_2\right] \cdot \left[\begin{array}{c|c} N_{n_z\delta_z} - \left(\dfrac{x_{\mathrm{IMU}}}{g}\right)M_{q\delta_z} & 0 \\ 0 & N_{n_z\delta_z} + \left(\dfrac{x_{\mathrm{IMU}}}{g}\right)M_{r\delta_y} \end{array}\right] \cdot \mathbf{T}(\phi_{\mathrm{f}}) \tag{16d}$$

actuators, accelerometers and gyrometers, with additional amplitude and rate saturation levels $\delta_{sat} = \pm 30°$ and $\dot{\delta}_{sat} = \pm 100°/s$ for the actuators. Uncertainty represents here unstructured high-frequency neglected dynamics [30].

Autopilot Design

The same $\mathcal{H}_\infty$ loop-shaping controller design approach [22, 23] detailed in the following section is applied for designing a robust structured controller, first for the nose roll-channel angular position dynamics, and second for the more complex projectile pitch/yaw-channel dynamics linearized at any equilibrium fixed operating point. The pitch/yaw-channel gain-scheduled controller is also described.

$\mathcal{H}_\infty$ Loop-Shaping Controller Design Methodology

The $\mathcal{H}_\infty$ loop-shaping controller design method comprises two main distinct steps, named as *open-loop shaping* and *robust stabilization*. As seen in Fig. 2, the first step consists in attaining a desired level of closed-loop performance by shaping over frequency, using pre- and post-filters $\mathbf{W}_1(s), \mathbf{W}_2(s)$ for the initial open-loop system $\mathbf{G}_K(s)$, the singular values of the open-loop system $\mathbf{G}_S(s) = \mathbf{W}_2(s)\,\mathbf{G}_K(s)\,\mathbf{W}_1(s)$. Typically, high gains at low frequencies and low gains at high frequencies are desirable for reference tracking/disturbance rejection and for noise attenuation, respectively, with no excessive roll-off ($\simeq 20$ dB/dec) at intermediate frequencies around the crossover frequency.

The second step is dedicated to robustness optimization by calculating an $\mathcal{H}_\infty$ controller $\mathbf{K}_\infty(s)$ robustly stabilizing $\mathbf{G}_S(s)$ with respect to unstructured normalized coprime factor (NCF) uncertainties. The maximal stability margin ε_{max} potentially reached can be calculated exactly and before robust controller computation. This margin indicates the success of loop-shaping: an $\varepsilon_{max} \ll 1$ means an incompatibility between performance and robustness specifications and the pre- and post-filters must be adapted; an $\varepsilon_{max} \gtrsim 0.3$ is satisfactory. A good value for ε_{max} also indicates that the open-loop shaped plant singular values should not be degraded too much by the robust controller. Finally, the global implemented controller is obtained as $\mathbf{K}(s) = \mathbf{W}_1(s)\,\mathbf{K}_\infty(s)\,\mathbf{W}_2(s)$.

The previous design technique is an alternative to standard $\mathcal{H}_\infty$ closed-loop shaping methods [41, 30], since the performance and robustness requirements are treated separately. It also tends to produce more robust controllers, since for robustness optimization those minimize implicitly the $\mathcal{H}_\infty$-norm of a set of four closed-loop sensitivity functions with each of them being associated with a specific uncertainty type.

Open-Loop Shaping

The definition of an open-loop shaped plant $\mathbf{G}_S(s)$ is here facilitated using the results of a first mixed-sensitivity $\mathcal{H}_\infty$ controller synthesis [17, 41, 30] incorporating a model-matching constraint [14] whose design setup is given in Fig. 3. In the linearized-based gain-scheduling control context for pitch/yaw dynamics autopilot design, this technique is relatively easy to adapt automatically to the synthesis point. In addition, since the same fixed control structure can be imposed for any operating condition using the $\mathcal{H}_\infty$ non-smooth optimization techniques proposed in [1], similar performance properties can be obtained over the whole projectile trimming envelope. Interpolation and implementation of the designed local controllers are also simplified.

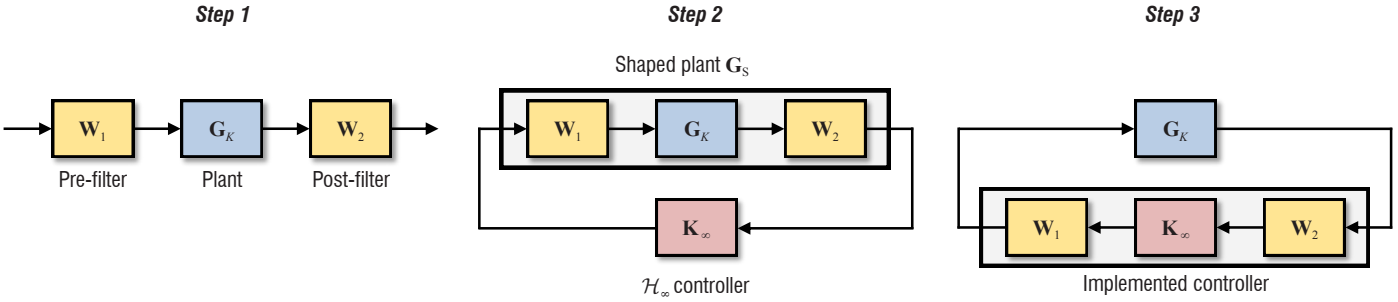

Figure 2 – The $\mathcal{H}_\infty$ loop-shaping controller design procedure

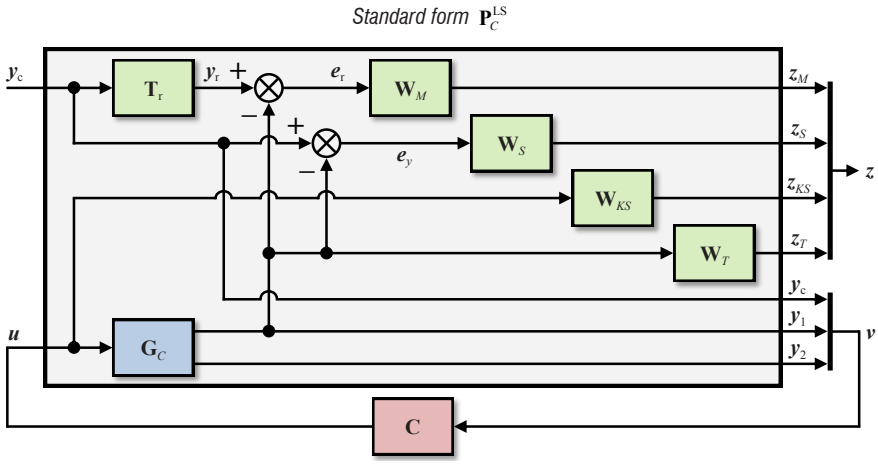

Figure 3 – Mixed-sensitivity $\mathcal{H}_\infty$ controller synthesis block diagram for open-loop shaping

The $\mathcal{H}_\infty$ synthesis problem of Fig. 3 consists in computing a controller $\mathbf{C}(s)$ with output $\boldsymbol{u}(s)$ and inputs $\boldsymbol{v}(s)=[\boldsymbol{y}_c(s)\ \ \boldsymbol{y}_1(s)\ \ \boldsymbol{y}_2(s)]^T$ containing a reference signal $\boldsymbol{y}_c(s)$, a tracking output $\boldsymbol{y}_1(s)$ and an additional measured output $\boldsymbol{y}_2(s)$, in order to maintain nominal (no uncertainty) internal stability and to guarantee that the closed-loop transfer function from the exogenous input $\boldsymbol{w}(s)=\boldsymbol{y}_c(s)$ to the performance outputs $\boldsymbol{z}(s)=[\boldsymbol{z}_S(s)\ \ \boldsymbol{z}_{KS}(s)\ \ \boldsymbol{z}_T(s)\ \ \boldsymbol{z}_M(s)]^T$ satisfies the following standard condition, given a performance index $\gamma>0$ to be minimized [41, 30]:

$$\left\|\mathbf{T}_{zw}^{\mathrm{LS}}(s)\right\|_\infty=\left\|\mathcal{F}_l\left[\mathbf{P}_C^{\mathrm{LS}}(s),\mathbf{C}(s)\right]\right\|_\infty=\left\|\begin{bmatrix}\mathbf{W}_M(s)\mathbf{M}(s)\\ \mathbf{W}_S(s)\mathbf{S}(s)\\ \mathbf{W}_{KS}(s)\mathbf{KS}(s)\\ \mathbf{W}_T(s)\mathbf{T}(s)\end{bmatrix}\right\|_\infty<\gamma \quad (17)$$

where the augmented nominal open-loop standard form $\mathbf{P}_C^{\mathrm{LS}}(s)$ is the interface between, on the one hand, the exogenous inputs and the controller outputs and, on the other hand, the performance outputs and controller inputs. The latter system comprises the nominal open-loop plant $\mathbf{G}_C(s)$ and a target closed-loop model $\mathbf{T}_r(s)$ used for model matching. It also contains the weighting filters $\mathbf{W}_M(s),\mathbf{W}_S(s),\mathbf{W}_{KS}(s)$ and $\mathbf{W}_T(s)$ which are used for shaping over frequency, in accordance with the desired closed-loop time and frequency objectives, the singular values of the closed-loop transfer functions related to the model-matching error $\boldsymbol{e}_r(s)=\boldsymbol{y}_r(s)-\boldsymbol{y}_1(s)$ (model-matching sensitivity $\mathbf{M}(s)$), tracking error $\boldsymbol{e}_y(s)=\boldsymbol{y}_c(s)-\boldsymbol{y}_1(s)$ (sensitivity $\mathbf{S}(s)$), control input $\boldsymbol{u}(s)$ (control sensitivity $\mathbf{KS}(s)$), and tracking output $\boldsymbol{y}_1(s)$ (complementary sensitivity $\mathbf{T}(s)$), respectively.

If the sensitivity functions meet the design requirements, an open-loop shaped plant $\mathbf{G}_S(s)=\mathbf{W}_2(s)\,\mathbf{G}_K(s)\,\mathbf{W}_1(s)$ is obtained by opening the closed-loop system $\mathbf{T}_{y_1w}^{\mathrm{LS}}(s)$. The latter, which results from connecting the designed controller $\mathbf{C}(s)$ to the plant $\mathbf{G}_C(s)$ to be controlled, is the closed-loop transfer function between the exogenous reference $\boldsymbol{w}(s)=\boldsymbol{y}_c(s)$ and the tracking output $\boldsymbol{y}_1(s)$ of the block diagram in Fig. 3.

The closed-loop system $\mathbf{T}_{y_1w}^{\mathrm{LS}}(s)$ is here broken at the level of the tracking error $\boldsymbol{e}_y(s)$. The initial open-loop system $\mathbf{G}_K(s)$ contains the plant to be controlled $\mathbf{G}_C(s)$, along with elements of the controller $\mathbf{C}(s)$, whereas the pre- and post-filters $\mathbf{W}_1(s),\mathbf{W}_2(s)$ only comprise controller elements. In addition, the point where the closed-loop system is broken corresponds to the point where the $\mathcal{H}_\infty$ controller $\mathbf{K}_\infty(s)$ is subsequently included.

2DoF $\mathcal{H}_\infty$ NLCF Robust Stabilization

The open-loop shaped plant $\mathbf{G}_S(s)$ is factored as:

$$\mathbf{G}_S(s)=\mathbf{M}_S^{-1}(s)\,\mathbf{N}_S(s),\ \text{with}\ \ \mathbf{M}_S(s)\in\mathbb{R}\mathcal{H}_\infty,\mathbf{N}_S(s)\in\mathbb{R}\mathcal{H}_\infty \quad (18)$$

where $\mathbf{M}_S(s),\mathbf{N}_S(s)$ are stable normalized left coprime factors (NLCF). A family $\mathcal{G}_{S,\Delta}$ of perturbed open-loop shaped plants $\mathbf{G}_{S,\Delta}(s)$ defined about the nominal open-loop shaped plant $\mathbf{G}_S(s)$ and reflecting the modeling uncertainty is given by:

$$\mathcal{G}_{S,\Delta}=\left\{\begin{array}{l}\mathbf{G}_{S,\Delta}(s)=\left[\mathbf{M}_S(s)+\boldsymbol{\Delta}_M(s)\right]^{-1}\left[\mathbf{N}_S(s)+\boldsymbol{\Delta}_N(s)\right]:\\ \left\|\left[\boldsymbol{\Delta}_N(s),-\boldsymbol{\Delta}_M(s)\right]\right\|_\infty<\varepsilon\end{array}\right\} \quad (19)$$

where the stable unknown unstructured perturbations $\boldsymbol{\Delta}_M(s),\boldsymbol{\Delta}_N(s)$ represent the uncertainty. The objective of $\mathcal{H}_\infty$ NLCF robust stabilization is to calculate a controller $\mathbf{K}_\infty(s)$ stabilizing both the nominal $\mathbf{G}_S(s)$ and any perturbed $\mathbf{G}_{S,\Delta}(s)$ open-loop shaped plants, and also verifying the following robustness condition with $\gamma>0$ minimized:

$$\left\|\begin{bmatrix}\mathbf{K}_\infty(s)\\ \mathbb{I}\end{bmatrix}\left\{\mathbb{I}-\mathbf{G}_S(s)\mathbf{K}_\infty(s)\right\}^{-1}\mathbf{M}_S^{-1}(s)\right\|_\infty=\gamma\le\varepsilon^{-1} \quad (20)$$

The stability margin $1/\gamma$ obtained with the controller $\mathbf{K}_\infty(s)$ is upper bounded by the maximum achievable stability margin $\varepsilon_{\max}=1/\gamma_{\min}$, which is calculated exactly as a function of the NLCF $\mathbf{M}_S(s),\mathbf{N}_S(s)$ as follows:

$$\varepsilon_{\max}=\sqrt{1-\left\|\left[\mathbf{N}_S(s),\mathbf{M}_S(s)\right]\right\|_H^2}>0 \quad (21)$$

where $\|\cdot\|_H$ denotes the Hankel norm.

In this work, robust stabilization with an $\mathcal{H}_\infty$ controller $\mathbf{K}_\infty(s)$ leads to significantly degrading the closed-loop system time-domain performance properties initially obtained with a good open-loop shaping. A solution is to devise a 2DoF controller for the set $\mathcal{G}_{S,\Delta}$ of perturbed open-loop shaped plants with input $\boldsymbol{u}_S(s)$ and output $\boldsymbol{y}_S(s)=\boldsymbol{y}_1(s)$ due to the structure chosen above for $\mathbf{G}_S(s)$, generally at the expense of an increase in the stability margin. The 2DoF controller $\mathbf{K}_{f\infty}(s)=[\mathbf{K}_f(s)\ \ \mathbf{K}_\infty(s)]$ here possesses the structure of Fig. 4, comprising a robustifying controller $\mathbf{K}_\infty(s)$ acting on the tracking error $\boldsymbol{e}_y(s)$ and an injection filter $\mathbf{K}_f(s)$ used for recovering the time-domain performance specified by the target system $\mathbf{T}_r(s)$.

A stabilizing structured 2DoF controller $\mathbf{K}_{f\infty}(s)$ is designed, again using the algorithms of [1], to minimize the $\mathcal{H}_\infty$-norm of the closed-loop system from the exogenous reference $\boldsymbol{y}_c(s)$ and disturbance $\boldsymbol{d}_{NM}(s)=\boldsymbol{d}_N(s)+\boldsymbol{d}_M(s)$ inputs symbolizing the NLCF uncertainty to the performance outputs $\boldsymbol{z}_N(s),\boldsymbol{z}_M(s),\boldsymbol{z}_r(s)$, where $\boldsymbol{z}_r(s)$ is the model-matching error: $\left\|\mathbf{T}_{zw}^{\mathrm{RS2}}(s)\right\|_\infty\le\gamma$ with $\gamma>0$. The parameter η permits the designer to adapt the weighted reference signal $\boldsymbol{y}_{c,\eta}(s)=\eta\cdot\boldsymbol{y}_c(s)$, in order to place more or less emphasis on model-matching at the expense of robustness.

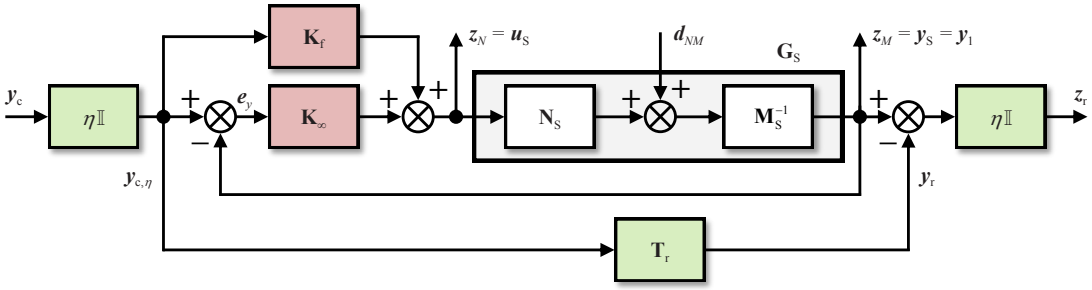

Figure 4 – 2DoF $\mathcal{H}_\infty$ robustifying controller synthesis block diagram

Robust stability is guaranteed if the closed-loop system $\mathrm{T}^{\mathrm{RS2}}_{z_{NM}d_{NM}}(s)$ from the disturbance input $\boldsymbol{d}_{NM}(s)$ to the performance output $\boldsymbol{z}_{NM}(s)=[z_N(s)\ \ \boldsymbol{z}_M(s)]^{\mathrm{T}}$ satisfies the following condition:

$$\left\|\mathrm{T}^{\mathrm{RS2}}_{z_{NM}d_{NM}}(s)\right\|_{\infty}=\gamma^{\star}\leq\varepsilon^{-1},\quad\text{with}\ \ \gamma>\gamma^{\star}>0 \tag{22}$$

where $\gamma^{\star}$ is the obtained stability margin.

Roll-Channel Autopilot

The complete nose roll-channel autopilot structure illustrated in Fig. 5 is composed of two cascaded loops. The internal fast loop contains the *rate controller* $K_p(s)$ that is used for reducing the nose rate $p_{\mathrm{f,f}}(t)$ following the reference signal $p_{\mathrm{f,c}}(t)$, during the ballistic flight subphase ($t_{\mathrm{start}}\leq t<t_{\mathrm{switch}}$). The preceding rate loop also aids the outer slow loop containing the *position controller* $\mathbf{K}_{\phi}(s)$ to ensure tracking of the reference position $\phi_{\mathrm{f,c}}(t)$ during the guided phase ($t_{\mathrm{switch}}\leq t\leq t_{\mathrm{impact}}$). The two controllers are designed separately, with the rate controller obtained first and the position one subsequently computed using the compensated internal rate control loop.

The design of a SISO PID rate controller $K_p(s)$ using the classical loop-shaping approach [30] is not detailed here for brevity purposes. This controller is sufficient to provide good performance properties in terms of robustness, as well as reference tracking and disturbance rejection, as shown from the nonlinear simulation results given at the end of the paper. A position controller $\mathbf{K}_{\phi}(s)$, which must satisfy critical and stringent performance and robustness specifications, is calculated by applying the particular $\mathcal{H}_{\infty}$ loop-shaping design technique proposed in the previous Subsection "$\mathcal{H}_{\infty}$ Loop-Shaping Controller Design Methodology".

The uncertain open-loop transfer function $\tilde{\mathbf{G}}_{\mathrm{R}}(s)$ of the uncertain LTI model of Eqs. (12)-(14) can be written as follows:

$$\begin{bmatrix}\dfrac{\phi_{\mathrm{f}}(s)}{p_{\mathrm{f,f}}(s)}\end{bmatrix}=\tilde{\mathbf{G}}_{\mathrm{R}}(s)\begin{bmatrix}\boldsymbol{d}(s)\\ V_{\mathrm{e}}(s)\end{bmatrix}=\left[\tilde{\mathbf{G}}_{\mathrm{R},d}(s)\ \middle|\ \tilde{\mathbf{G}}_{\mathrm{R},u}(s)\right]\begin{bmatrix}\boldsymbol{d}(s)\\ V_{\mathrm{e}}(s)\end{bmatrix} \tag{23}$$

where the control $\tilde{\mathbf{G}}_{\mathrm{R},u}(s)$ and disturbance $\tilde{\mathbf{G}}_{\mathrm{R},d}(s)$ dynamics are expressed as:

$$\left[\tilde{\mathbf{G}}_{\mathrm{R},d}(s)\ \middle|\ \tilde{\mathbf{G}}_{\mathrm{R},u}(s)\right]= \tag{24}$$
$$\left[\begin{array}{ccc|c}\tilde{G}_{\mathrm{R},\phi d_{\phi}}(s) & \tilde{G}_{\mathrm{R},\phi d_p}(s) & \tilde{G}_{\mathrm{R},\phi d_i}(s) & \tilde{G}_{\mathrm{R},\phi u}(s)\\ 0 & \tilde{G}_{\mathrm{R},pd_p}(s) & \tilde{G}_{\mathrm{R},pd_i}(s) & \tilde{G}_{\mathrm{R},pu}(s)\end{array}\right]$$

Only the control dynamics $\tilde{\mathbf{G}}_{\mathrm{R},u}(s)=[\tilde{G}_{\mathrm{R},\phi u}(s)\ \ \tilde{G}_{\mathrm{R},pu(s)}]^{\mathrm{T}}$ are used here to design a nose position controller, since the effects of the disturbances $\boldsymbol{d}(s)$ of Eq. (14) are insignificant.

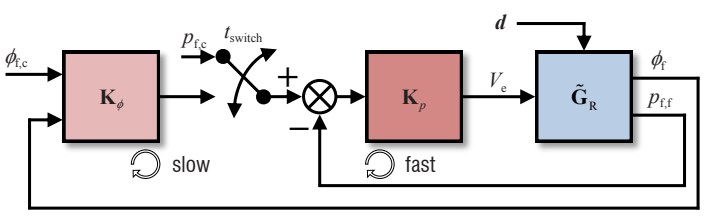

Figure 5 – Complete nose roll-channel autopilot architecture

Open-Loop Shaping

The design of a position controller uses the open-loop system $F_{\mathrm{R},\phi u}(s)$, which is obtained as the series interconnection of the nominal (no uncertainty) control dynamics of the compensated internal loop of Fig. 5 with the nominal position control dynamics $G_{\mathrm{R},\phi u}(s)$ and which is given by:

$$F_{\mathrm{R},\phi u}(s)=\frac{\phi_{\mathrm{f}}(s)}{p_{\mathrm{f,c}}(s)}=G_{\mathrm{R},\phi u}(s)\cdot\frac{K_p(s)}{1+G_{\mathrm{R},pu}(s)K_p(s)} \tag{25}$$

Following the general $\mathcal{H}_{\infty}$ linear controller design setup of Fig. 3, where the open-loop system $G_C(s)=F_{\mathrm{R},\phi u}(s)$ has $u(s)=p_{\mathrm{f,c}}(s)$ as input and $y_1(s)=\phi_{\mathrm{f}}(s)$ as tracking output (no additional output $y_2(s)$). With the reference signal $y_{\mathrm{c}}(s)=\phi_{\mathrm{f,c}}(s)$, the controller inputs are $\boldsymbol{v}(s)=[y_{\mathrm{c}}(s)\ \ y_1(s)]^{\mathrm{T}}=[\phi_{\mathrm{f,c}}(s)\ \ \phi_{\mathrm{f}}(s)]^{\mathrm{T}}$ and the tracking error $e_y(s)=e_{\phi}(s)=\phi_{\mathrm{f,c}}(s)-\phi_{\mathrm{f}}(s)$. The target model $T_{\mathrm{r}}(s)=T_{\phi,\mathrm{r}}(s)$ with input $\phi_{\mathrm{f,c}}(s)$ and output $y_{\mathrm{r}}(s)=\phi_{\mathrm{f,r}}(s)$ is chosen as a second-order filter with a desired natural frequency $\omega_{\phi,\mathrm{r}}=14.5$ rad/s and a damping ratio $\xi_{\phi,\mathrm{r}}=0.79$, giving a settling time $t_{\phi,\mathrm{s}}=0.254$ s for a 2% envelope around steady state. The settling time $t_{\phi,\mathrm{s}}$ is taken as sufficiently large compared to that of the nose-channel internal rate loop and sufficiently small compared to that of the projectile pitch/yaw-channel control loop without leading to saturation of the coaxial motor.

Controller design is here performed by shaping only the closed-loop model-matching, sensitivity and control sensitivity functions using the following model-matching filter $W_M(s)$:

$$W_M(s)=\frac{\frac{1}{k_M}s+\omega_M}{s+\omega_M\varepsilon_M} \tag{26}$$

whose inverse is a high-pass filter, since the model-matching transfer function frequency content is in the shape of a bell centered on the intermediate frequencies (see Fig. 7b). The error between the responses of the target and shaped closed-loop transfer functions is reduced as much as possible at low frequencies in order to ensure a good reference tracking and, at intermediate frequencies, to improve the transient response. The values given to the parameters ε_M and k_M adequately adjust the gain of $W_M^{-1}(s)$ at low and high frequencies, respectively, whereas the critical parameter ω_M, initially set to the target closed-loop system bandwidth $\omega_{\phi,\mathrm{c}}$, is used to adapt the cutoff frequency. The tracking error filter $W_S(s)$ is chosen as:

$$W_S(s)=\frac{s^2+2\xi_{\phi,\mathrm{r}}\omega_{\phi,\mathrm{r}}s+\omega_{\phi,\mathrm{r}}^2}{s^2+2\xi_{\phi,\mathrm{r}}\omega_{\phi,\mathrm{r}}s+\varepsilon_S} \tag{27}$$

whose inverse is equal to the 2nd-order low-pass filter $S_{\phi,\mathrm{r}}(s)=1-T_{\phi,\mathrm{r}}(s)$, in which a small $\varepsilon_S>0$ is added to obtain a stable filter. The weighting $W_S(s)$ is used to adjust the closed-loop system bandwidth, steady-state error and overshoot. The control filter $W_{KS}(s)$ is defined as:

$$W_{KS}(s)=\left(\frac{k_{KS}\varepsilon_{KS}}{\omega_{KS}}\right)\cdot\frac{s+\omega_{KS}}{s+\varepsilon_{KS}} \tag{28}$$

whose inverse is a 1st-order low-pass filter with a static gain k_{KS}^{-1}, a bandwidth ω_{KS} and a high-frequency negative real zero ensured by $\varepsilon_{KS}>0$ and used to obtain a proper and stable weighting $W_{KS}(s)$. The control signal weight limits the control bandwidth at high frequencies by adjusting ω_{KS}, initially fixed to $\omega_{\phi,\mathrm{c}}$, in order to limit the risk of coaxial motor saturations.

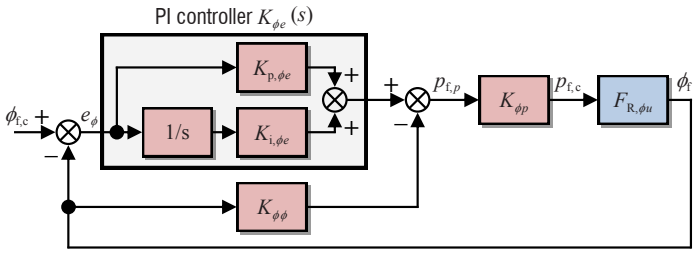

Figure 6 – Structure of the nose position PI-P controller $\mathbf{C}(s)$

Controller synthesis results

The designed reduced-order (RO) controller $\mathbf{C}(s)$ of Fig. 3 possesses the PI-P (proportional-integral & proportional) structure illustrated in detail in Fig. 6. It comprises a tracking error PI servo-controller $K_{\phi e}(s)$, an output feedback regulation proportional gain $K_{\phi\phi}$ and a roll-off/protection 1st-order filter $K_{\phi p}(s)$. The control signal is given by:

$$p_{f,c}(s) = K_{\phi p}(s)\left\{K_{\phi e}(s)\phi_{f,c}(s) - \left[K_{\phi e}(s) + K_{\phi\phi}\right]\phi_f(s)\right\} \quad (29)$$

with:

$$K_{\phi e}(s) = \frac{K_{p,\phi e}\, s + K_{i,\phi e}}{s} \quad (30a)$$

$$K_{\phi p}(s) = \frac{1}{\tau_{\phi p} s + 1} \quad (30b)$$

Figures 7a-7d give the RO and fixed structure controller synthesis results (blue), which are compared to those obtained for the design of a full-order (FO) controller (magenta). The target (red) and shaped (magenta for FO and blue for RO controllers) closed-loop transfer functions possess the desired properties conforming to robust control theory [11, 30]. For the sensitivities $\mathbf{S}(s)$, the small low-frequency gains indicate a very good minimization of the steady-state tracking error and the peak at intermediate frequencies, which remains small, leads to a good robustness with respect to unstructured inverse multiplicative uncertainties. For the model-matching sensitivities $\mathbf{M}(s)$, the small gains, in particular at intermediate frequencies, show a good target model following. For the control sensitivities $\mathbf{KS}(s)$ that present a peak around the desired closed-loop system bandwidth $\omega_{\phi,c}$, those possess a good roll-off from the intermediate frequencies avoiding large controller gains and limiting the control bandwidth, and hence maintaining moderate actuator usage. Finally, for the complementary sensitivities $\mathbf{T}(s)$, the low-frequency gains close to 0 dB also indicate the excellent steady-state tracking error reduction, the absence of a peak at intermediate frequencies denotes robustness with respect to unstructured multiplicative uncertainties, and small high-frequency gains help with measurement noise attenuation.

Open-loop shaped plant

A nominal RO open-loop shaped plant $G_S(s) = W_2 G_K(s)\, W_1(s)$, which is illustrated in Fig. 8, is here defined by breaking the closed-loop system of Fig. 6 at the level of the tracking error $e_\phi(s)$, as

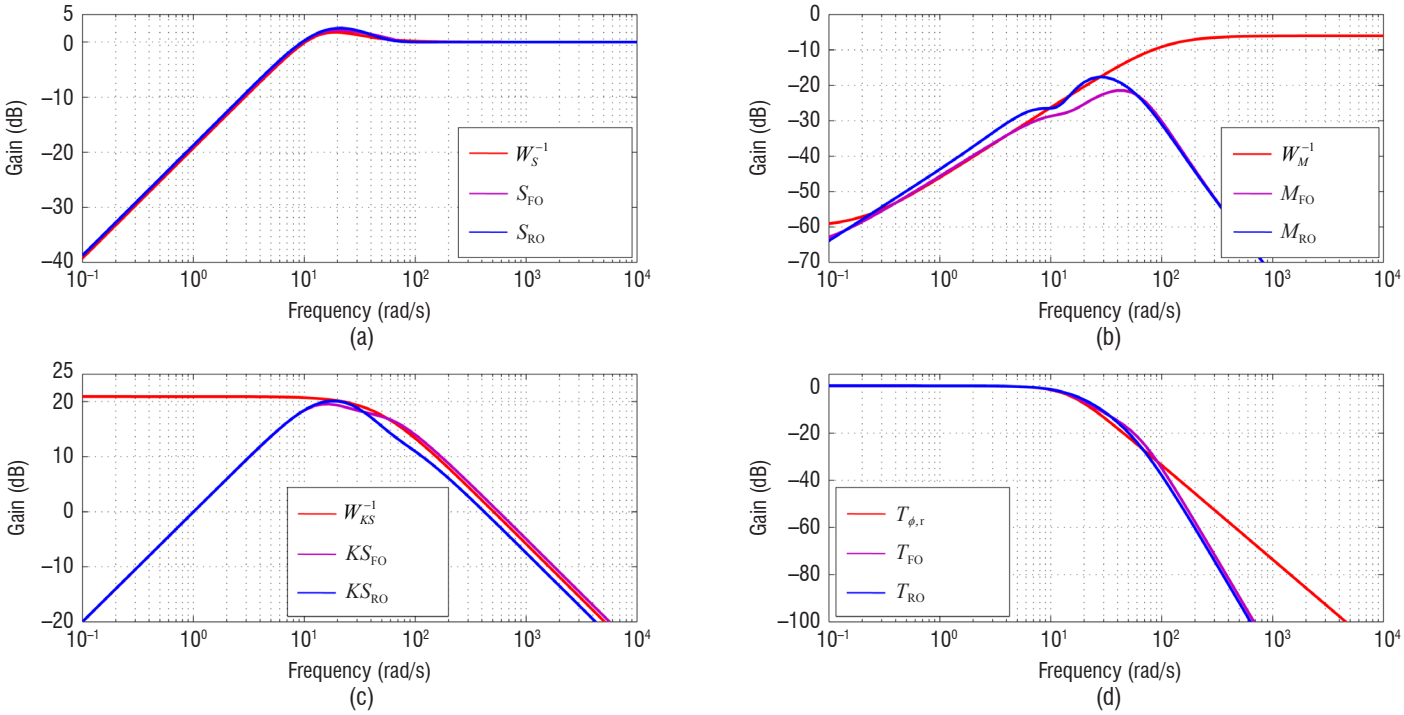

Figure 7 – Frequency responses of the position loop target (red) and shaped (magenta: FO, blue: RO) closed-loop transfer functions related to the: (a) tracking error $e_\phi(s)$, (b) model-matching error $e_r(s)$, (c) control $p_{f,c}(s)$, (d) output $\phi_f(s)$ signals

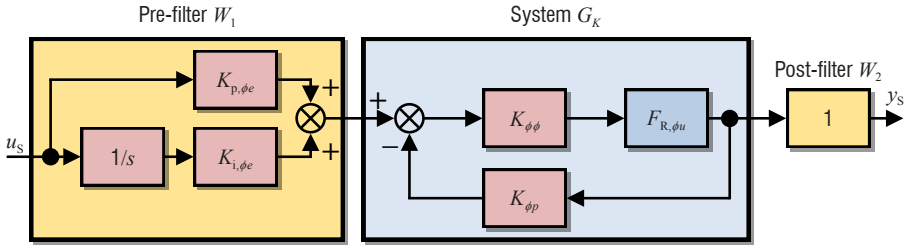

Figure 8 – Open-loop shaped plant $G_S(s) = W_2 G_K(s)\, W_1(s)$ block diagram

explained in Subsection "$\mathcal{H}_\infty$ Loop-Shaping Controller Design Methodology". The gain of $G_{\mathrm{S}}(s)$ (blue), along with that of a similar FO open-loop shaped plant built with the closed-loop system containing the FO controller (magenta), are shown in Fig. 9 and compared to the initial open-loop system $F_{\mathrm{R},\phi u}(s)$ (black). The RO and FO open-loop shaped plants have close gains with desired properties, and possess crossover frequencies larger than that of the open-loop system denoting a faster system response obtained thanks to open-loop shaping. Finally, the very good value $\varepsilon_{\max} = 0.5942$ is achieved for the maximum stability margin associated with $G_{\mathrm{S}}(s)$.

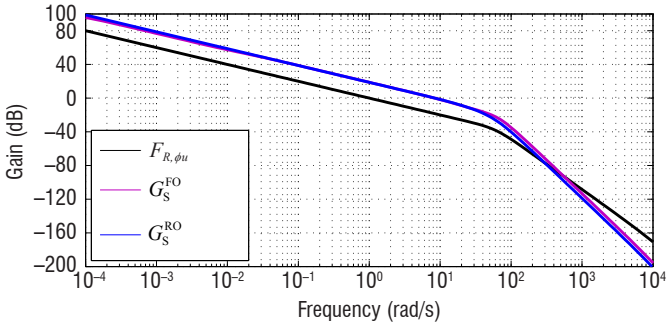

Figure 9 – Gains of the open-loop system $F_{\mathrm{R},\phi u}(s)$ (black), and of the FO (magenta) and RO (blue) open-loop shaped plants $G_{\mathrm{S}}^{\mathrm{FO}}(s)$ and $G_{\mathrm{S}}^{\mathrm{RO}}(s)$

2DoF NLCF $\mathcal{H}_\infty$ Robust Stabilization

A 2DoF fixed structure and reduced order controller $\mathbf{K}_{\phi\mathrm{f}\infty}(s)$, which is calculated for the open-loop shaped plant $G_{\mathrm{S}}(s)$ depicted in Fig. 8 using the linear controller design setup of Fig. 4, here comprises a robustifying gain $K_{\phi\infty}$ and an injection 1st-order lead-lag filter $K_{\phi\mathrm{f}}(s)$ with time constants $\tau_{\phi\mathrm{f}}^{\mathrm{lead}}$ and $\tau_{\phi\mathrm{f}}^{\mathrm{lag}}$ and defined as:

$$K_{\phi\mathrm{f}}(s) = \frac{\tau_{\phi\mathrm{f}}^{\mathrm{lead}}\, s + 1}{\tau_{\phi\mathrm{f}}^{\mathrm{lag}}\, s + 1} \tag{31}$$

The target system $T_{\phi,\mathrm{r}}(s)$ is used again for NLCF $\mathcal{H}_\infty$ robust stabilization, and controller tuning using $\eta = 0.1$ gives the reasonable performance index $\gamma_{\mathrm{RO2}} = 1.8473$. The actually achieved stability margin $\varepsilon_{\mathrm{RO2}} = 1/\gamma_{\mathrm{RO2}}^{\star} = 0.5487$ is excellent and close both to the stability margin $\varepsilon_{\mathrm{FO2}} = 1/\gamma_{\mathrm{FO2}}^{\star} = 0.5933$ obtained with a robustifying FO 2DoF controller and to the very good maximum stability margin $\varepsilon_{\max} = 0.5942$. Consequently, the degradation of the low and high-frequency gains of the initial open-loop shaped plant $G_{\mathrm{S}}(s)$ is very limited.

The complete external nose-channel position 2DoF structured controller $\mathbf{K}_{\phi}(s)$ of Fig. 5 is obtained by combining the PI-P controller $\mathbf{C}(s)$ used for open-loop shaping, along with the 2DoF robustifying RO controller $\mathbf{K}_{\phi\mathrm{f}\infty}(s)$, as illustrated in detail in Fig. 10. A static pre-filter $K_{\phi\mathrm{sc}}$ is added after robust stabilization, in order to ensure a unitary steady-state gain for the closed-loop transfer function between the reference $\phi_{\mathrm{f,c}}(s)$ and the output $\phi_{\mathrm{f}}(s)$ signals, given the integral action in the PI-P controller. This pre-filter is obtained as follows:

$$K_{\phi\mathrm{sc}} = \frac{K_{\phi\infty}}{K_{\phi\infty} + K_{\phi\mathrm{f}}(s)\big|_{s=0}} \tag{32}$$

The control signal $p_{\mathrm{f,c}}(s)$ is given by:

$$\begin{aligned} p_{\mathrm{f,c}}(s) = {} & K_{\phi p}(s) K_{\phi e}(s) \left\{ K_{\phi\mathrm{f}}(s) + K_{\phi\infty} \right\} K_{\phi\mathrm{sc}}\, \phi_{\mathrm{f,c}}(s) \\ & - K_{\phi p}(s) \left\{ K_{\phi e}(s) K_{\phi\infty} + K_{\phi\phi} \right\} \phi_{\mathrm{f}}(s) \end{aligned} \tag{33}$$

The singular value of the complete nose position 2DoF RO controller $\mathbf{K}_{\phi}(s)$ (green) possesses a limited bandwidth with a good roll-off at high frequencies, as shown in Fig. 11. It also remains close to the singular values of the PI-P controller used for open-loop shaping (black), and of a 2DoF controller built with the PI-P and the robustifying 2DoF FO controllers (magenta).

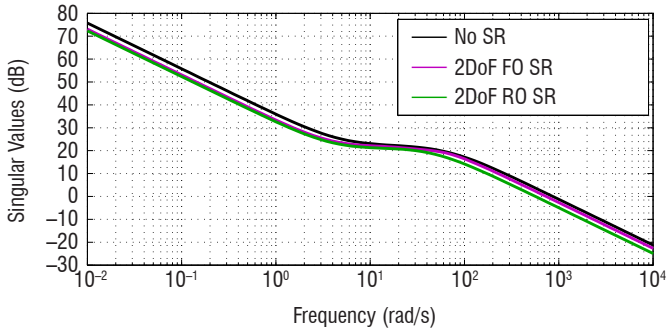

Figure 11 – Singular values of the nose position controllers: without any robustifying 2DoF controller (black), with the robustifying 2DoF FO controller (magenta), and with the robustifying 2DoF RO controller (green)

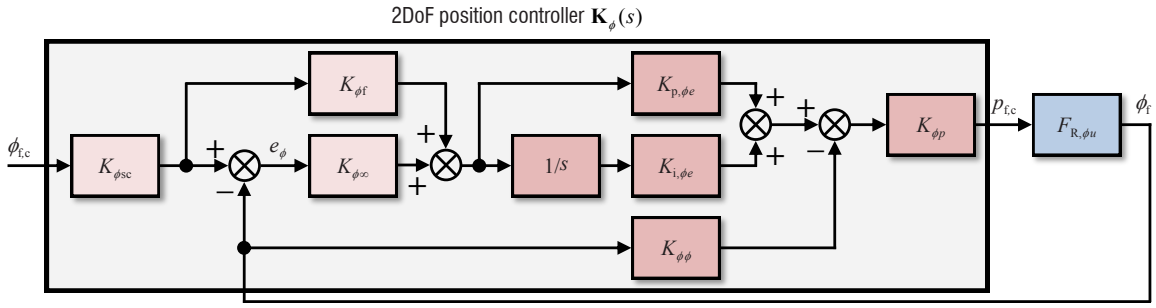

Figure 10 – 2DoF structure of the nose position controller $\mathbf{K}_{\phi}(s)$

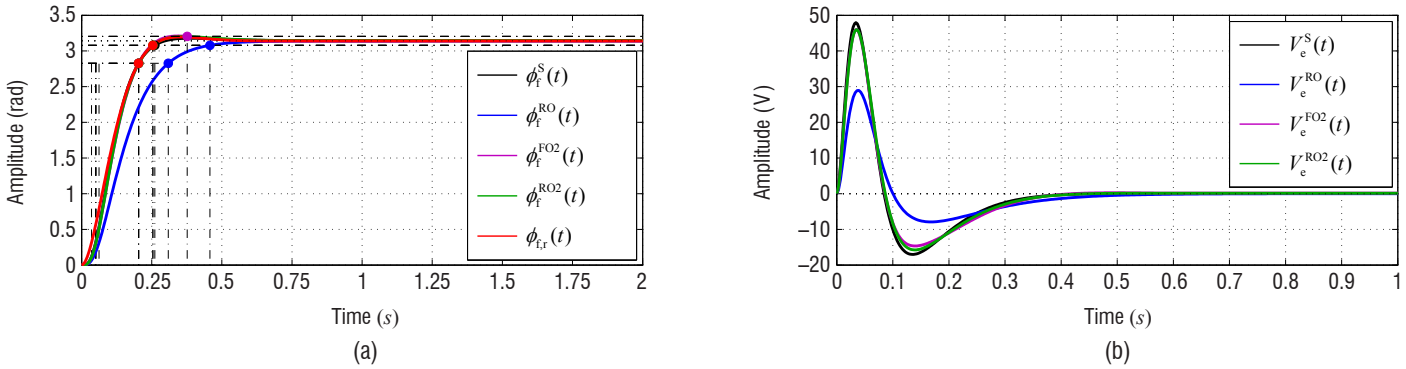

Figure 12 – Closed-loop step responses: (a) roll angle $\phi_{\mathrm{f}}(t)$, (b) actuator input voltage $V_{\mathrm{e}}(t)$

Finally, Figs. 12a, 12b give the step responses for the transfer functions of the complete nose position control loop of Fig. 10, which are related to the output $\phi_{\mathrm{f}}(t)$ and voltage $V_{\mathrm{e}}(t)$ (green), for a step amplitude of π rad corresponding to the maximal value potentially taken by $\phi_{\mathrm{f,c}}(t)$ at the beginning of the projectile flight guided phase. In Fig. 12a, the output-related time response follows very well the target system response (red), contrary to that of a closed-loop system obtained with the open-loop shaped plant $G_{\mathrm{S}}(s)$ and a 1DoF robustifying controller (blue). Hence, the time performance initially obtained for the closed-loop system used for open-loop shaping (black) is perfectly recovered. The use of the robustifying 2DoF FO controller does not give satisfactory performance results. In Fig. 12b, the voltage $V_{\mathrm{e}}(t)$ applied to the coaxial motor remains reasonable.

Robust Stability Analysis

The preceding complete nose position autopilot is tested for robust stability, first with respect to an NLCF uncertainty block $[\boldsymbol{\Delta}_N(s), \boldsymbol{\Delta}_M(s)]$, using the robustness criterion of the $\mathcal{H}_\infty$ loop shaping design procedure. The estimated size $\varepsilon = 0.0627$ of this unstructured uncertainty, which corresponds to the various uncertain parameters considered in the nose-channel dynamics linear model of Eq. (12), verifies $\varepsilon \leq \varepsilon_{\mathrm{RO2}} = 0.5413$ and hence robust stability is guaranteed[1].

Robust stability is also tested by applying the μ-analysis theory tools [41, 30] to the uncertain closed-loop system $\tilde{\mathbf{T}}_{\phi_{\mathrm{f}}\phi_{\mathrm{f,c}}}(s) = \mathcal{F}_{\mathrm{l}}[\tilde{\mathbf{P}}_K(s), \mathbf{K}_\phi(s)]$ associated with the nominal closed-loop model of Fig. 10. The uncertain open-loop augmented plant $\tilde{\mathbf{P}}_K(s)$ enclosing all of the real parametric uncertainties can be written as the u-LFT of a nominal open-loop system $\mathbf{P}_K^{\Delta}(s)$ and of a stable, diagonal, real, normalized parametric perturbation $\boldsymbol{\Delta}$ as:

$$\tilde{\mathbf{P}}_K(s) = \mathcal{F}_{\mathrm{u}}[\mathbf{P}_K^{\Delta}(s), \boldsymbol{\Delta}] \tag{34}$$

with:

$$\boldsymbol{\Delta} = \left\{ \mathrm{diag}\left[\delta_{K_{\mathrm{a}}}\mathbb{I}_1, \delta_{K_{\mathrm{b}}}\mathbb{I}_1, \delta_{K_{\mathrm{m}}}\mathbb{I}_1, \delta_{K_{\mathrm{v}}}\mathbb{I}_1, \delta_L\mathbb{I}_1, \delta_R\mathbb{I}_1 \right] : |\delta_i| \leq 1, \delta_i \in \mathbb{R} \right\} \tag{35}$$

The uncertain closed-loop system $\tilde{\mathbf{T}}_{\phi_{\mathrm{f}}\phi_{\mathrm{f,c}}}(s)$ can hence be obtained as the following *l*-LFT:

$$\begin{aligned} \tilde{\mathbf{T}}_{\phi_{\mathrm{f}}\phi_{\mathrm{f,c}}}(s) &= \mathcal{F}_{\mathrm{u}}\left[\mathbf{N}_K^{\Delta}(s), \boldsymbol{\Delta} \right] \\ &\triangleq \mathbf{N}_K^{\Delta,22}(s) + \mathbf{N}_K^{\Delta,21}(s)\boldsymbol{\Delta}\left[\mathbb{I} - \mathbf{N}_K^{\Delta,11}(s)\boldsymbol{\Delta} \right]^{-1} \mathbf{N}_K^{\Delta,12}(s) \end{aligned} \tag{36}$$

where the nominal system $\mathbf{N}_K^{\Delta}(s)$, internally stabilized by the controller $\mathbf{K}_\phi(s)$, is given by:

$$\mathbf{N}_K^{\Delta}(s) = \mathcal{F}_{\mathrm{l}}\left[\mathbf{P}_K^{\Delta}(s), \mathbf{K}_\phi(s) \right] \tag{37}$$

The only source of instability in the uncertain closed-loop system of Eq. (36) can originate from the feedback term $[\mathbb{I} - \mathbf{N}_K^{\Delta,11}(s)\boldsymbol{\Delta}]^{-1}$ between the stable systems $\mathbf{M}_K^{\Delta}(s) = \mathbf{N}_K^{\Delta,11}(s)$ and $\boldsymbol{\Delta}$. Robust stability (RS) of the uncertain closed-loop system with respect to the uncertainty $\boldsymbol{\Delta}$ is guaranteed if and only if:

$$\mathrm{RS} \Leftrightarrow \mu_{\Delta}\left[\mathbf{M}_K^{\Delta}(j\omega) \right] < 1, \quad \forall \omega \in \mathbb{R}^+ \tag{38}$$

where $\mu_{\Delta}(\cdot)$ is the structured singular value (SSV).

Upper and lower bounds for the SSV are numerically calculated over a frequency grid for the levels of parametric uncertainties presented in Subsection "Roll-Channel" of Part "Airframe Modeling". Given that the upper bound is always smaller than 1, as seen in Fig. 13, RS is confirmed with an important stability margin here.

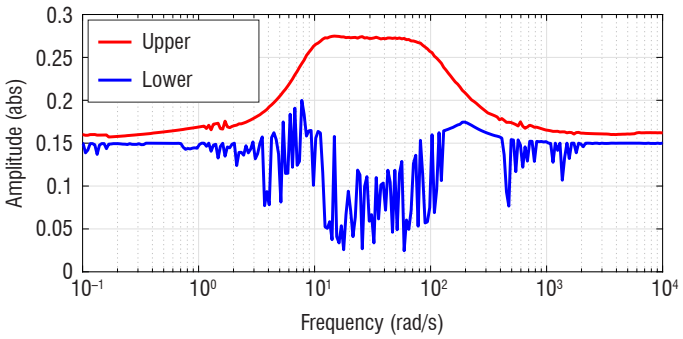

Figure 13 – Upper and lower SSV bounds calculated for the uncertain closed-loop system

[1] It is worth noting that a good robustness to coprime uncertainty to the open-shaped plant $G_{\mathrm{S}}(s)$ of Fig. 8 does not necessarily lead to good robustness margins at the input and outputs of the actual nominal control dynamics plant $\mathbf{G}_{\mathrm{R},u}(s)$ given by Eqs. (23), (24), the latter plant being contained in the system $F_{\mathrm{R},\phi u}(s)$ given by Eq. (25). Satisfactory multi-loop disk gain and phase margins [4] are, however, obtained here at the actual plant input (MDG = ±10.4 dB and MDP = ±56.4°) and outputs (MDG = ±3.7 dB and MDP = ±24.1°).

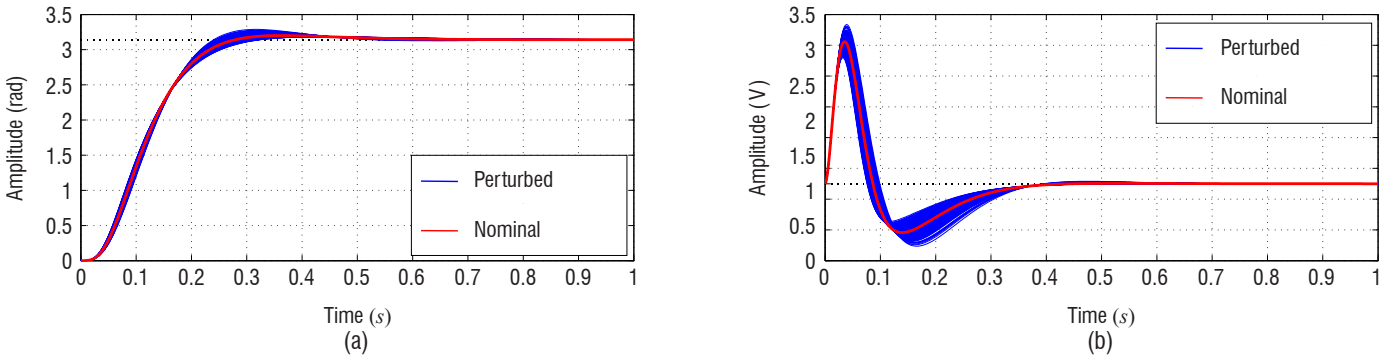

Figure 14 – Uncertain closed-loop system step responses: (a) roll angle, (b) actuator voltage

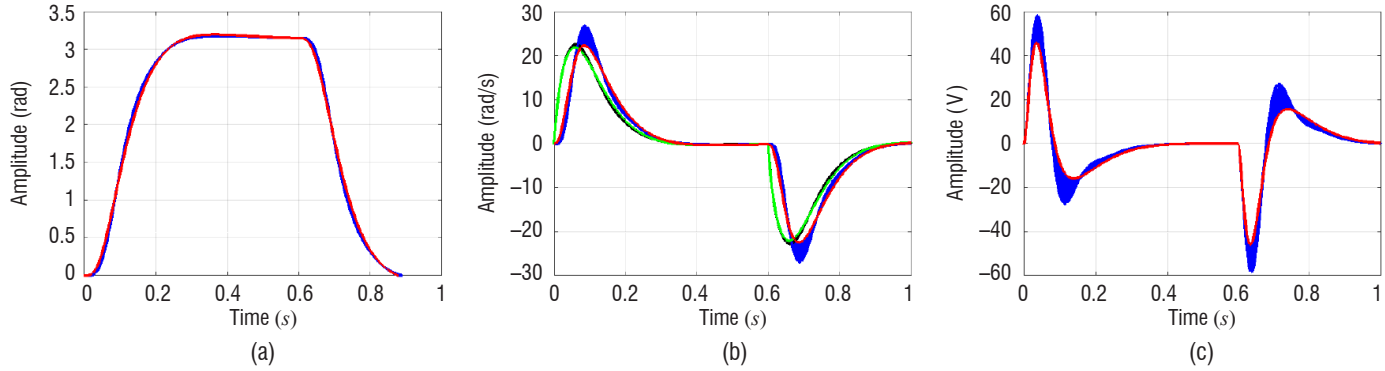

Figure 15 – Closed-loop time responses with transmission delays at actuator input: (a) roll angle (blue: perturbed, red: nominal), (b) reference (black: perturbed, green: nominal) and output (blue: perturbed, red: nominal) roll rates, (c) actuator voltage (blue: perturbed, red: nominal)

Two additional linear simulation results are given in Figs. 14, 15. The first figure depicts nose-channel output angle $\phi_{\mathrm{f}}(t)$ and actuator voltage $V_{\mathrm{e}}(t)$ step responses of 200 uncertain closed-loop system random samples, from which robust stability can be verified again and no excessive input voltage to the coaxial motor is demanded. The second figure shows step responses related to the output roll position and rate $\phi_{\mathrm{f}}(t), p_{\mathrm{f,f}}(t)$, internal loop input roll rate $p_{\mathrm{f,c}}(t)$, and voltage $V_{\mathrm{e}}(t)$, given actuator input transmission delays of up to 9 ms, *i.e.*, around 5 times a rate of 1/600 s with which the control signal could be sampled. Stability is preserved, the degradations appearing on the different time responses remain more or less limited with respect to the nominal case, and there is no actuator saturation. Hence, the nose position control loop can handle realistic delays of up to 3 times the control signal sampling rate [32], *i.e.*, 5 ms.

Pitch/Yaw-Channel Autopilot

Augmented Plant for Controller Synthesis

Autopilot design for the pitch/yaw-channel dynamics linearized at any operating point is based on the open-loop actuator/projectile/sensor dynamics *q*-LPV model described in Subsection "Pitch/Yaw-Channels" of Part "Airframe Modeling". The load factor output measurements are actually provided at the projectile nose, and hence those do not match the necessary feedback signals, which must be available here at the projectile CM, since the nonlinear force dynamic equations are written for this point. The load factor feedback signals are calculated at the CM through a transformation based on an inverse Grubin transformation [40] and using the measured load factor and angular rate outputs. The angular rate measurements remain valid for any point of the projectile. The transformation system $\mathbf{T}^{\rho}_{n\omega}(s,\boldsymbol{\rho}_{\mathrm{PY}})$, which calculates in the non-rolling frame B′ CS at the CM the load factors $\breve{\boldsymbol{n}}_{\mathrm{zy},\varepsilon}(s)=[\breve{n}_{\mathrm{z},\varepsilon}(s)\ \breve{n}_{\mathrm{y},\varepsilon}(s)]^{\mathrm{T}}$ and angular rates $\breve{\boldsymbol{\omega}}_{qr,\varepsilon}(s)=[\breve{q}_{\varepsilon}(s)\ \breve{r}_{\varepsilon}(s)]^{\mathrm{T}}$, from the measurements $\boldsymbol{n}_{\mathrm{zy},\varepsilon,\mathrm{m}}(s)=[n_{\mathrm{z},\varepsilon,\mathrm{m}}(s)\ n_{\mathrm{y},\varepsilon,\mathrm{m}}(s)]^{\mathrm{T}}$ and $\boldsymbol{\omega}_{qr,\varepsilon,\mathrm{m}}(s)=[q_{\varepsilon,\mathrm{m}}(s)\ r_{\varepsilon,\mathrm{m}}(s)]^{\mathrm{T}}$ obtained in the nose frame $\mathrm{B_f}$ CS, is defined as:

$$\begin{aligned}\begin{bmatrix}\breve{n}_{\mathrm{z},\epsilon}(s)\\ \breve{n}_{\mathrm{y},\epsilon}(s)\end{bmatrix}&=\mathbf{T}(\phi_{\mathrm{f}})\mathbf{W}_{\mathrm{b},n}(s,\boldsymbol{\lambda}_{\mathrm{PY}})\begin{bmatrix}n_{\mathrm{z},\epsilon,\mathrm{m}}(s)\\ n_{\mathrm{y},\epsilon,\mathrm{m}}(s)\end{bmatrix}\\&-\left(\frac{x_{\mathrm{IMU}}}{g}\right)p_{\mathrm{f,f}}(s)\mathbf{T}(\phi_{\mathrm{f}})\mathbf{W}_{\mathrm{b},\omega}(s,\boldsymbol{\lambda}_{\mathrm{PY}})\begin{bmatrix}r_{\epsilon,\mathrm{m}}(s)\\ q_{\epsilon,\mathrm{m}}(s)\end{bmatrix}\\&+\left(\frac{x_{\mathrm{IMU}}}{g}\right)\mathbf{W}_{\mathrm{d},\omega}(s,\boldsymbol{\lambda}_{\mathrm{PY}})\overline{\mathbf{T}}(\phi_{\mathrm{f}})\mathbf{W}_{\mathrm{b},\omega}(s,\boldsymbol{\lambda}_{\mathrm{PY}})\begin{bmatrix}q_{\epsilon,\mathrm{m}}(s)\\ r_{\epsilon,\mathrm{m}}(s)\end{bmatrix}\end{aligned}\tag{39a}$$

$$\begin{bmatrix}\breve{q}_{\epsilon}(s)\\ \breve{r}_{\epsilon}(s)\end{bmatrix}=\overline{\mathbf{T}}(\phi_{\mathrm{f}})\mathbf{W}_{\mathrm{b},\omega}(s,\boldsymbol{\lambda}_{\mathrm{PY}})\begin{bmatrix}q_{\epsilon,\mathrm{m}}(s)\\ r_{\epsilon,\mathrm{m}}(s)\end{bmatrix}\tag{39b}$$

with the matrix $\mathbf{T}(\phi_{\mathrm{f}})$ given in Eq. (6). The diagonal parameter-dependent 1st-order approximated derivative filters $\mathbf{W}_{\mathrm{d},\omega}(s,\boldsymbol{\lambda}_{\mathrm{PY}})=\mathrm{diag}[W_{\mathrm{d},\omega}(s,\boldsymbol{\lambda}_{\mathrm{PY}}),-W_{\mathrm{d},\omega}(s,\boldsymbol{\lambda}_{\mathrm{PY}})]$ are applied to the angular rates, and the identical diagonal parameter-dependent 2nd-order low-pass filters $\mathbf{W}_{\mathrm{b},n}(s,\boldsymbol{\lambda}_{\mathrm{PY}})=\mathbf{W}_{\mathrm{b},\omega}(s,\boldsymbol{\lambda}_{\mathrm{PY}})=\mathrm{diag}[W_{\mathrm{b}}(s,\boldsymbol{\lambda}_{\mathrm{PY}}),W_{\mathrm{b}}(s,\boldsymbol{\lambda}_{\mathrm{PY}})]$, which are obtained as the product of two 1st-order systems, are used for measurement noise attenuation. Tuning the parameters of the previous filters is critical due to their significant influence on closed-loop system performance and robust stability.

Finally, controller synthesis following the strategy presented in Subsection "$\mathcal{H}_{\infty}$ Loop-Shaping Controller Design Methodology" is performed with an augmented open-loop uncertain plant $\tilde{\mathbf{G}}_{\mathrm{PY}}(s,\boldsymbol{\lambda}_{\mathrm{PY}})$, which is composed of the simplified *q*-LPV model of the uncertain actuator/projectile/sensor dynamics parameterized by $\boldsymbol{\lambda}_{\mathrm{PY}}=[V\ \ h]^{\mathrm{T}}$, and of a simplified transformation system $\mathbf{T}^{\lambda}_{n\omega}(s,\boldsymbol{\lambda}_{\mathrm{PY}})$ obtained by imposing $(\phi_{\mathrm{f}},p_{\mathrm{f,f}})=(0,0)$ in Eqs. (39). The multivariable plant $\tilde{\mathbf{G}}_{\mathrm{PY}}(s,\boldsymbol{\lambda}_{\mathrm{PY}})$,

having the actuator commands $\boldsymbol{\delta}_{\mathrm{mn},\varepsilon,\mathrm{c}}(s)$ as inputs and the feedback signals $\breve{\boldsymbol{n}}_{\mathrm{zy},\varepsilon}(s), \breve{\boldsymbol{\omega}}_{qr,\varepsilon}(s)$ as outputs, contains zeros in its SISO load factor transfer functions that are potentially NMP as a function of the operating condition. These zeros are, however, sufficiently fast compared to the desired closed-loop bandwidth, contrary to those of the projectile pitch/yaw-channel dynamics (see Subsection "Pitch/Yaw-Channels" of Part "Airframe Modeling").

Open-Loop Shaping

The various systems and signals, appearing in the $\mathcal{H}_\infty$ linear controller design diagram of Fig. 3 used here for defining at any fixed synthesis point $\overline{\boldsymbol{\lambda}}_{\mathrm{PY}}$ a pitch/yaw-channel open-loop shaped plant, are explicitly presented. The system to control $\mathbf{G}_C(s)$ is equal to the augmented plant $\breve{\mathbf{G}}_{\mathrm{PY}}(s,\overline{\boldsymbol{\lambda}}_{\mathrm{PY}}) = [\breve{\mathbf{G}}_{\mathrm{PY},n}(s,\overline{\boldsymbol{\lambda}}_{\mathrm{PY}}), \breve{\mathbf{G}}_{\mathrm{PY},\omega}(s,\overline{\boldsymbol{\lambda}}_{\mathrm{PY}})]^{\mathrm{T}}$ with input $\boldsymbol{u}(s) = \boldsymbol{\delta}_{\mathrm{mn},\varepsilon,\mathrm{c}}(s)$ and outputs $\boldsymbol{y}_1(s) = \breve{\boldsymbol{n}}_{\mathrm{zy},\varepsilon}(s), \boldsymbol{y}_2(s) = \breve{\boldsymbol{\omega}}_{qr,\varepsilon}(s)$. The target model $\mathbf{T}_{\mathrm{r}}(s)$, with input $\boldsymbol{y}_{\mathrm{c}}(s) = \boldsymbol{n}_{\mathrm{zy},\varepsilon,\mathrm{c}}(s) = [n_{\mathrm{z,c}}(s)\ \ n_{\mathrm{y,c}}(s)]^{\mathrm{T}}$ and output $\boldsymbol{y}_{\mathrm{r}}(s) = \boldsymbol{n}_{\mathrm{zy},\varepsilon,\mathrm{r}}(s) = [\boldsymbol{n}_{\mathrm{z,r}}(s)\ \ \boldsymbol{n}_{\mathrm{y,r}}(s)]^{\mathrm{T}}$, is a block-diagonal 2nd-order system $\mathbf{T}_{n,\mathrm{r}}(s) = \mathrm{diag}[T_{n,\mathrm{r}}(s), T_{n,\mathrm{r}}(s)]$ with a natural frequency $\omega_{n,\mathrm{r}} = 4.9\,\mathrm{rad/s}$ and a damping ratio $\xi_{n,\mathrm{r}} = 0.79$ giving a settling time $t_{n,\mathrm{s}} = 0.751\,\mathrm{s}$ for a 2% envelope around steady state. The obtained pitch/yaw-channel closed system response is hence sufficiently fast without saturating the canard actuators, while being sufficiently slow with respect to the nose-channel position control loop response.

The parameter-dependent model-matching $\mathbf{W}_M(s,\overline{\boldsymbol{\lambda}}_{\mathrm{PY}}) = \mathrm{diag}[W_M(s,\overline{\boldsymbol{\lambda}}_{\mathrm{PY}}), W_M(s,\overline{\boldsymbol{\lambda}}_{\mathrm{PY}})]$ and the performance $\mathbf{W}_S(s) = \mathrm{diag}[W_S(s), W_S(s)]$ weights are defined as for nose position autopilot design, whereas the control signal weight $\mathbf{W}_{KS}(s,\overline{\boldsymbol{\lambda}}_{\mathrm{PY}}) = \mathrm{diag}[W_{KS}(s,\overline{\boldsymbol{\lambda}}_{\mathrm{PY}}), W_{KS}(s,\overline{\boldsymbol{\lambda}}_{\mathrm{PY}})]$ is:

$$W_{KS}\left(s,\overline{\boldsymbol{\lambda}}_{\mathrm{PY}}\right) = \left(\frac{s+\omega_{KS}\left(\overline{\boldsymbol{\lambda}}_{\mathrm{PY}}\right)k_{KS}^{1/2}\left(\overline{\boldsymbol{\lambda}}_{\mathrm{PY}}\right)}{\varepsilon_{KS}^{-1/2}s+\omega_{KS}\left(\overline{\boldsymbol{\lambda}}_{\mathrm{PY}}\right)}\right)^2 \tag{40}$$

The inverse of $W_{KS}(s,\overline{\boldsymbol{\lambda}}_{\mathrm{PY}})$ is equal to the product of two identical 1st-order low-pass filters with a steady-state gain $k_{KS}^{-1/2}(\overline{\boldsymbol{\lambda}}_{\mathrm{PY}})$, a bandwidth adjusted with $\omega_{KS}(\overline{\boldsymbol{\lambda}}_{\mathrm{PY}})$, and a high-frequency negative real zero ensured by $\varepsilon_{KS} > 0$ and making the weight proper and stable. For any synthesis point $\overline{\boldsymbol{\lambda}}_{\mathrm{PY}}$, the steady-state gain $k_{KS}^{-1}(\overline{\boldsymbol{\lambda}}_{\mathrm{PY}})$ of $W_{KS}(s,\overline{\boldsymbol{\lambda}}_{\mathrm{PY}})$ is conditioned by the low-frequency minimal singular value of the synthesis system: $k_{KS}(\overline{\boldsymbol{\lambda}}_{\mathrm{PY}}) \simeq \underline{\sigma}[\breve{\mathbf{G}}_{\mathrm{PY}}(0,\overline{\boldsymbol{\lambda}}_{\mathrm{PY}})]$. The frequency $\omega_{KS}(\overline{\boldsymbol{\lambda}}_{\mathrm{PY}})$, which is initially set to the target closed-loop system bandwidth $\omega_{n,\mathrm{r}} = 4.9\,\mathrm{rad/s}$, can be increased for specific operating conditions where a faster control signal is needed, such as, for example, at a low airspeed/high altitude flight point. Finally, the output signal weight $\mathbf{W}_T(s) = \mathrm{diag}[W_T(s), W_T(s)]$ is defined as:

$$W_T\left(s\right) = \frac{s^2+2\xi_{n,\mathrm{r}}\,\omega_{n,\mathrm{r}}s+\omega_{n,\mathrm{r}}^2}{\omega_{n,\mathrm{r}}^2\left(\varepsilon_T^{-1}s+1\right)^2} \tag{41}$$

The filter $W_T(s)$ is the result of inverting the target system and adding two high-frequency negative real poles $\varepsilon_T > 0$ to render it proper and stable. The output signal weight leads to attenuating noise on the feedback output load factors $\breve{\boldsymbol{n}}_{\mathrm{zy},\varepsilon}$ and helps both the performance filter to minimize the steady-state error $\boldsymbol{e}_n(s)$ and the model-matching filter to reduce the difference between the target and shaped closed-loop system at intermediate frequencies.

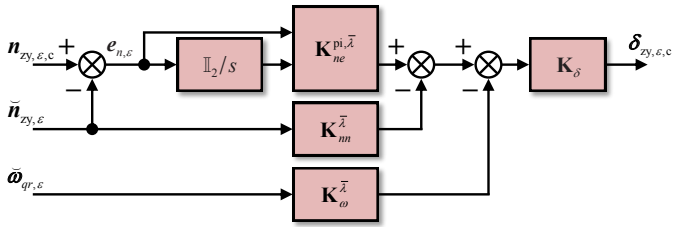

Figure 16 – PI-P-P structure of the pitch/yaw-channel linear controller $\mathbf{C}(s,\overline{\boldsymbol{\lambda}}_{\mathrm{PY}})$

Controller synthesis results

The PI-P-P fixed and RO structure chosen for the controller $\mathbf{C}(s)$ of Fig. 3 comprises four blocks, as shown by Fig. 16: a tracking error PI servo-controller $\mathbf{K}_{ne}(s,\overline{\boldsymbol{\lambda}}_{\mathrm{PY}})$ containing the gain matrix $\mathbf{K}_{ne}^{\mathrm{pi}}(\overline{\boldsymbol{\lambda}}_{\mathrm{PY}})$, two output feedback regulation proportional controllers $\mathbf{K}_{nn}(\overline{\boldsymbol{\lambda}}_{\mathrm{PY}})$ and $\mathbf{K}_{\omega}(\overline{\boldsymbol{\lambda}}_{\mathrm{PY}})$ applied to the output load factors and angular rates, respectively, and finally a block-diagonal roll-off and actuator protection filter $\mathbf{K}_{\delta}(s)$ composed of 1st-order low-pass systems. The control signal $\boldsymbol{\delta}_{\mathrm{zy},\varepsilon,\mathrm{c}}(s)$ is given by:

$$\boldsymbol{\delta}_{\mathrm{zy},\varepsilon,\mathrm{c}}\left(s\right) = \mathbf{K}_{\delta}\left(s\right)\left[\mathbf{K}_{ne}^{\overline{\boldsymbol{\lambda}}}\left(s\right), -\mathbf{K}_{ne}^{\overline{\boldsymbol{\lambda}}}\left(s\right) - \mathbf{K}_{nn}^{\overline{\boldsymbol{\lambda}}}, -\mathbf{K}_{\omega}^{\overline{\boldsymbol{\lambda}}}\right]\begin{bmatrix}\boldsymbol{n}_{\mathrm{zy},\varepsilon,\mathrm{c}}\left(s\right)\\ \breve{\boldsymbol{n}}_{\mathrm{zy},\varepsilon}\left(s\right)\\ \breve{\boldsymbol{\omega}}_{qr,\varepsilon}\left(s\right)\end{bmatrix} \tag{42}$$

where, *i.e.*, $\mathbf{K}_{ne}^{\overline{\boldsymbol{\lambda}}}(s) = \mathbf{K}_{ne}(s,\overline{\boldsymbol{\lambda}}_{\mathrm{PY}})$, and with:

$$\begin{aligned}\mathbf{K}_{ne}\left(s,\overline{\boldsymbol{\lambda}}_{\mathrm{PY}}\right) = &\begin{bmatrix}K_{ne}^{\mathrm{p},11}\left(\overline{\boldsymbol{\lambda}}_{\mathrm{PY}}\right) & K_{ne}^{\mathrm{p},12}\left(\overline{\boldsymbol{\lambda}}_{\mathrm{PY}}\right)\\ K_{ne}^{\mathrm{p},12}\left(\overline{\boldsymbol{\lambda}}_{\mathrm{PY}}\right) & -K_{ne}^{\mathrm{p},11}\left(\overline{\boldsymbol{\lambda}}_{\mathrm{PY}}\right)\end{bmatrix}\\ &+\begin{bmatrix}K_{ne}^{\mathrm{i},11}\left(\overline{\boldsymbol{\lambda}}_{\mathrm{PY}}\right) & K_{ne}^{\mathrm{i},12}\left(\overline{\boldsymbol{\lambda}}_{\mathrm{PY}}\right)\\ K_{ne}^{\mathrm{i},12}\left(\overline{\boldsymbol{\lambda}}_{\mathrm{PY}}\right) & -K_{ne}^{\mathrm{i},11}\left(\overline{\boldsymbol{\lambda}}_{\mathrm{PY}}\right)\end{bmatrix}\begin{bmatrix}1/s & 0\\ 0 & 1/s\end{bmatrix}\end{aligned} \tag{43a}$$

$$\mathbf{K}_{nn}\left(\overline{\boldsymbol{\lambda}}_{\mathrm{PY}}\right) = \begin{bmatrix}K_{nn}^{11}\left(\overline{\boldsymbol{\lambda}}_{\mathrm{PY}}\right) & K_{nn}^{12}\left(\overline{\boldsymbol{\lambda}}_{\mathrm{PY}}\right)\\ K_{nn}^{12}\left(\overline{\boldsymbol{\lambda}}_{\mathrm{PY}}\right) & -K_{nn}^{11}\left(\overline{\boldsymbol{\lambda}}_{\mathrm{PY}}\right)\end{bmatrix} \tag{43b}$$

$$\mathbf{K}_{\omega}\left(\overline{\boldsymbol{\lambda}}_{\mathrm{PY}}\right) = \begin{bmatrix}K_{\omega}^{11}\left(\overline{\boldsymbol{\lambda}}_{\mathrm{PY}}\right) & K_{\omega}^{12}\left(\overline{\boldsymbol{\lambda}}_{\mathrm{PY}}\right)\\ -K_{\omega}^{12}\left(\overline{\boldsymbol{\lambda}}_{\mathrm{PY}}\right) & K_{\omega}^{11}\left(\overline{\boldsymbol{\lambda}}_{\mathrm{PY}}\right)\end{bmatrix} \tag{43c}$$

$$\mathbf{K}_{\delta}\left(s\right) = \begin{bmatrix}\dfrac{1}{\tau_{\delta}s+1} & 0\\ 0 & \dfrac{1}{\tau_{\delta}s+1}\end{bmatrix} \tag{43d}$$

The actual controls $\boldsymbol{\delta}_{\mathrm{mn},\varepsilon,\mathrm{c}}(s)$ sent to the canard actuators are computed from the virtual ones $\boldsymbol{\delta}_{\mathrm{zy},\varepsilon,\mathrm{c}}(s)$ using the matrix $\mathbf{T}(\phi_{\mathrm{f}})$ of Eq. (6). The preceding controller structure, including only gains and simple filters with particular symmetries, permits the designer to significantly reduce interpolation and implementation efforts and costs compared to a FO controller. The eight controller gains are tuned for any synthesis point, whereas the roll-off filter bandwidth remains fixed.

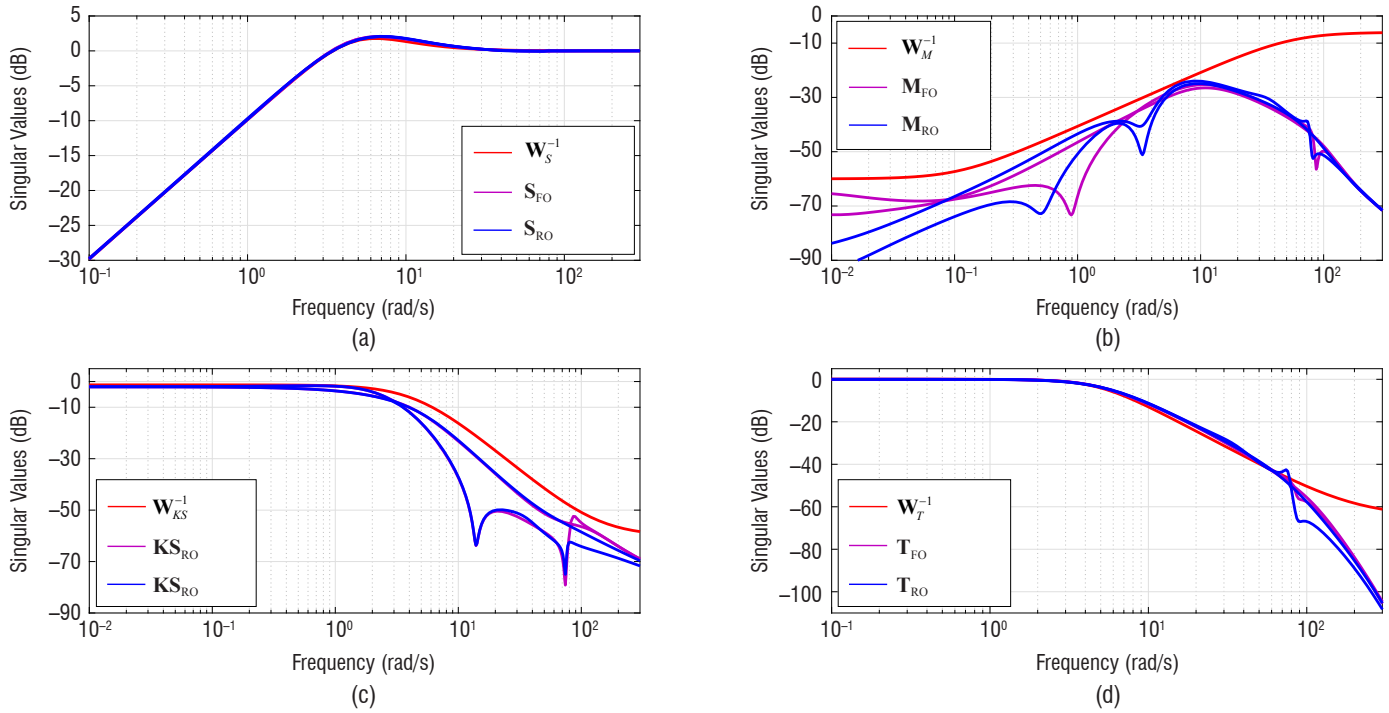

Figure 17 – Frequency responses of the target system (red) and shaped (magenta: FO, blue: RO) closed-loop transfer functions computed at the *critical point* and related to the: (a) tracking error $\boldsymbol{e}_{n,\varepsilon}(s)$, (b) model-matching error $\boldsymbol{e}_{\mathrm{r}}(s)$, (c) control $\boldsymbol{\delta}_{\mathrm{zy},\varepsilon,\mathrm{c}}(s)$, (d) output $\breve{\boldsymbol{n}}_{\mathrm{zy},\varepsilon}(s)$ signals

The RO and fixed-structure controller synthesis frequency results (blue) for a fixed critical low airspeed/high altitude operating point are illustrated in Figs. 17a-17d and compared to the results obtained with a FO controller (magenta). The various shaped closed-loop transfer functions verify the constraints imposed by the weighting filters (red), and hence possess the desired properties as in the case of nose position autopilot design (see Figs. 7a-7d).

Open-loop shaped plant

A nominal RO open-loop shaped plant $\mathbf{G}_{\mathrm{S}}(s)=\mathbf{W}_2\mathbf{G}_K(s)\mathbf{W}_1(s)$ defined by breaking the computed closed-loop system before the tracking error PI servo-controller is shown in Fig. 18. Figure 19 gives the singular values for the RO open-shaped plant (blue), for a FO one that is similarly defined using the previously calculated FO controller (magenta), and for the initial airframe load factor open-loop system $\breve{\mathbf{G}}_{\mathrm{PY},n}(s,\overline{\boldsymbol{\lambda}}_{\mathrm{PY}})$ (black). The RO and FO open-loop shaped plant singular values are close to each other, with desired properties. In addition, open-loop shaping leads to significantly dampening (more than 60 dB) the precession and nutation modes. Finally, the maximum stability margin calculated for the RO $\mathbf{G}_{\mathrm{S}}(s)$ plant is very good, with $\varepsilon_{\max}=0.6131$.

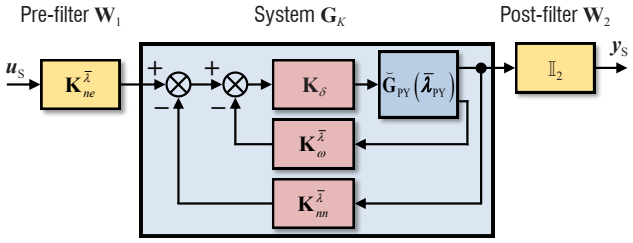

Figure 18 – Nominal open-loop shaped plant $\mathbf{G}_{\mathrm{S}}(s,\overline{\boldsymbol{\lambda}}_{\mathrm{PY}})=\mathbf{W}_2\mathbf{G}_K(s,\overline{\boldsymbol{\lambda}}_{\mathrm{PY}})\mathbf{W}_1(s,\overline{\boldsymbol{\lambda}}_{\mathrm{PY}})$

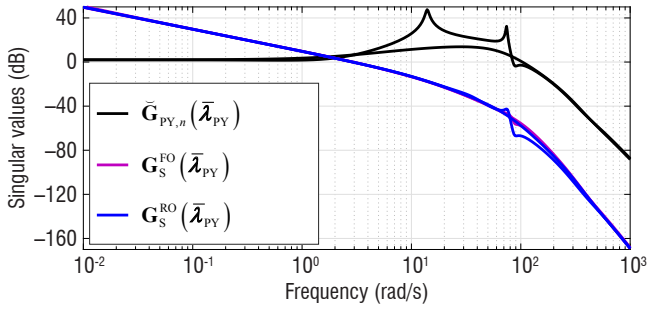

Figure 19 – Singular values of the open-loop load factor system $\breve{\mathbf{G}}_{\mathrm{PY},n}(s,\overline{\boldsymbol{\lambda}}_{\mathrm{PY}})$ (black), and of the FO (magenta) and RO (blue) open-loop shaped plants $\mathbf{G}_{\mathrm{S}}^{\mathrm{FO}}(s,\overline{\boldsymbol{\lambda}}_{\mathrm{PY}})$ and $\mathbf{G}_{\mathrm{S}}^{\mathrm{RO}}(s,\overline{\boldsymbol{\lambda}}_{\mathrm{PY}})$

2DoF NLCF $\mathcal{H}_\infty$ Robust Stabilization

A 2DoF $\mathcal{H}_\infty$ controller $\mathbf{K}_{nf\infty}(s)$ computed with the loop-shape of Fig. 18 using the controller design diagram of Fig. 4 is chosen with the parameter-dependent RO and fixed structure robustifying static part $\mathbf{K}_{n\infty}(\overline{\boldsymbol{\lambda}}_{\mathrm{PY}})=\mathrm{diag}[K_{n\infty}(\overline{\boldsymbol{\lambda}}_{\mathrm{PY}}),K_{n\infty}(\overline{\boldsymbol{\lambda}}_{\mathrm{PY}})]$ and injection dynamic part $\mathbf{K}_{nf}(s,\overline{\boldsymbol{\lambda}}_{\mathrm{PY}})=\mathrm{diag}[K_{nf}(s,\overline{\boldsymbol{\lambda}}_{\mathrm{PY}}),K_{nf}(s,\overline{\boldsymbol{\lambda}}_{\mathrm{PY}})]$. The latter is composed of two identical 1st-order lead-lag systems $K_{nf}(s,\overline{\boldsymbol{\lambda}}_{\mathrm{PY}})$ with a steady-state gain $k_{nf}(\overline{\boldsymbol{\lambda}}_{\mathrm{PY}})$ and time constants $\tau_{nf}^{\mathrm{lead}}(\overline{\boldsymbol{\lambda}}_{\mathrm{PY}}),\tau_{nf}^{\mathrm{lag}}(\overline{\boldsymbol{\lambda}}_{\mathrm{PY}})$:

$$K_{nf}\left(s,\overline{\boldsymbol{\lambda}}_{\mathrm{PY}}\right)=k_{nf}\left(\overline{\boldsymbol{\lambda}}_{\mathrm{PY}}\right)\cdot\frac{\tau_{nf}^{\mathrm{lead}}\left(\overline{\boldsymbol{\lambda}}_{\mathrm{PY}}\right)s+1}{\tau_{nf}^{\mathrm{lag}}\left(\overline{\boldsymbol{\lambda}}_{\mathrm{PY}}\right)s+1} \tag{44}$$

The parameters to be tuned are the controller $\mathbf{K}_{n\infty}(\overline{\boldsymbol{\lambda}}_{\mathrm{PY}})$ and the steady-state gain and time constants of the injection filter $\mathbf{K}_{nf}(s,\overline{\boldsymbol{\lambda}}_{\mathrm{PY}})$. For the same target model $\mathbf{T}_{n,\mathrm{r}}(s)$ as that used for open-loop shaping in the previous Subsection "Open-Loop Shaping" and $\eta=0.1$, controller parameter tuning at the critical low airspeed/high altitude operating point gives the very good performance index $\gamma_{\mathrm{RO2}}=1.7588$. The excellent stability margin $\varepsilon_{\mathrm{RO2}}=1/\gamma_{\mathrm{RO2}}^{\star}=0.5721$ remains close to a stability margin $\varepsilon_{\mathrm{FO2}}=1/\gamma_{\mathrm{FO2}}^{\star}=0.6114$ offered by a robustifying 2DoF FO controller and to the maximum stability margin $\varepsilon_{\max}=0.6131$.

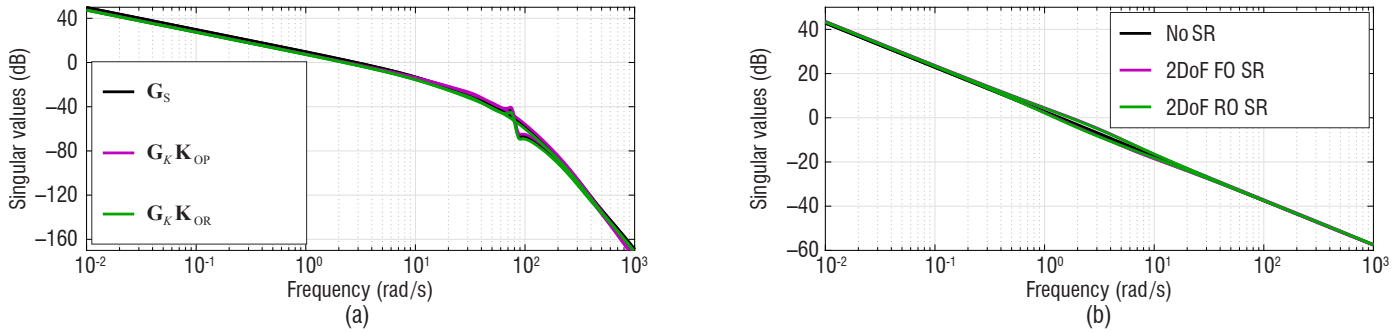

Figure 20 – Singular values of the: (a) desired $\mathbf{G}_S(s)$ (black), actual FO $\mathbf{G}_K\mathbf{K}_{FO}(s)$ (magenta) and actual RO $\mathbf{G}_K\mathbf{K}_{RO}(s)$ (green) loop-shapes; (b) pitch/yaw-channel linear controllers: without any robustifying controller (black), with the robustifying 2DoF FO controller (magenta), and with the robustifying 2DoF RO controller (green)

It can be then noticed, using the RO and FO actual open-loop shaped plants $\mathbf{G}_K\mathbf{K}_{RO}(s,\bar{\boldsymbol{\lambda}}_{PY})$ and $\mathbf{G}_K\mathbf{K}_{FO}(s,\bar{\boldsymbol{\lambda}}_{PY})$[2], which are obtained at system $\mathbf{G}_K(s)$ output and plotted in Fig. 20a, that the degradations at low and high frequencies in the initial open-loop shaped plant due to the $\mathcal{H}_\infty$ controller are very small.

The complete 2DoF RO and fixed structure obtained at any synthesis point for a pitch/yaw-channel linearized dynamics controller is shown in Fig. 21. It particularly comprises a parameter-dependent diagonal static pre-filter $\mathbf{K}_{nsc}(\bar{\boldsymbol{\lambda}}_{PY}) = \text{diag}[K_{nsc}(\bar{\boldsymbol{\lambda}}_{PY}), K_{nsc}(\bar{\boldsymbol{\lambda}}_{PY})]$, which is added after robust stabilization to ensure a unitary steady-state gain for the closed-loop transfer function between the reference $\boldsymbol{n}_{zy,\varepsilon,c}(s)$ and tracking output $\breve{\boldsymbol{n}}_{zy,\varepsilon}(s)$ signals, given the integral action in the PI controller. The expression of the diagonal components $K_{nsc}(\bar{\boldsymbol{\lambda}}_{PY})$ is similar to Eq. (32). The controller fixed structure, which remains simple and easy to interpolate and implement, generates the virtual control signal $\boldsymbol{\delta}_{zy,\varepsilon,c}(s)$ given by Eq. (45), in which, *i.e.*, $\mathbf{K}_\omega^{\bar{\lambda}} = \mathbf{K}_\omega(\bar{\boldsymbol{\lambda}}_{PY})$. The actuator commands $\boldsymbol{\delta}_{mn,\varepsilon,c}(s)$ are computed again using Eq. (6).

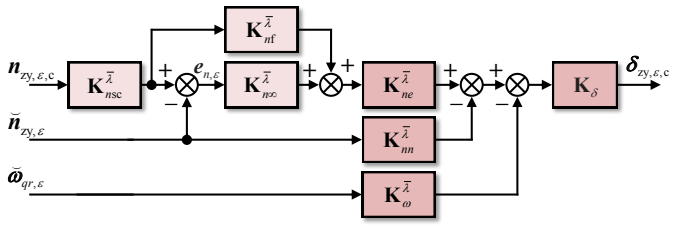

Figure 21 – 2DoF controller for the linearized pitch/yaw-channel dynamics

Figure 20b shows the singular values for the complete RO controller of Fig. 21 (green), for a complete FO controller containing the robustifying 2DoF FO controller instead (magenta), and for the PI-P-P controller of Fig. 16 used for open-loop shaping (black). All of the singular values remain close to each other and hence the good properties of the PI-P-P controller (low-frequency integral action, high-frequency sufficient roll-off, reasonable bandwidth) are well preserved.

Finally, Figs. 22a-22d illustrate the step responses for the transfer functions of the pitch/yaw-channel complete RO linear control loop

$$\boldsymbol{\delta}_{zy,\varepsilon,c}(s) = \mathbf{K}_\delta(s)\left[\mathbf{K}_{ne}^{\bar{\lambda}}(s)\left\{\mathbf{K}_{nf}^{\bar{\lambda}}(s)+\mathbf{K}_{n\infty}^{\bar{\lambda}}\right\}\mathbf{K}_{nsc}^{\bar{\lambda}} \;\middle|\; -\left\{\mathbf{K}_{ne}^{\bar{\lambda}}(s)\mathbf{K}_{n\infty}^{\bar{\lambda}}+\mathbf{K}_{nn}^{\bar{\lambda}}\right\} \quad -\mathbf{K}_{\omega}^{\bar{\lambda}}\right]\begin{bmatrix}\boldsymbol{n}_{zy,\varepsilon,c}(s)\\ \breve{\boldsymbol{n}}_{zy,\varepsilon}(s)\\ \breve{\boldsymbol{\omega}}_{qr,\varepsilon}(s)\end{bmatrix} \tag{45}$$

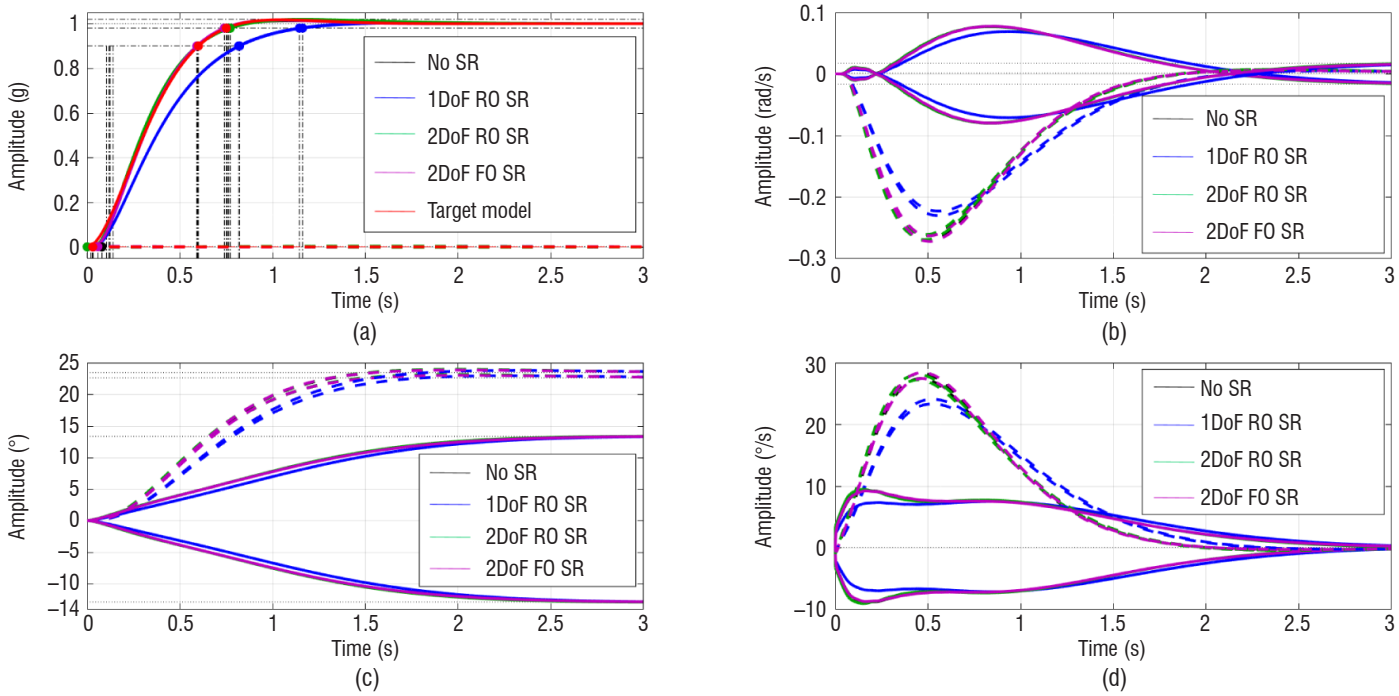

Figure 22 – Closed-loop step responses: (a) normalized load factor $\breve{\boldsymbol{n}}_{zy,\varepsilon}(t)$, (b) angular rate $\breve{\boldsymbol{\omega}}_{qr,\varepsilon}(t)$, (c) control $\boldsymbol{\delta}_{zy,\varepsilon,c}(t)$, (d) control rate $\dot{\boldsymbol{\delta}}_{zy,\varepsilon,c}(t)$ signals (solid: response on the same axis as the reference, dashed: response on the opposite axis to the reference)

[2] RO and FO actual loop-shapes: $\mathbf{G}_K\mathbf{K}_{RO} = \mathbf{G}_K\mathbf{W}_1\mathbf{K}_{n\infty}\mathbf{W}_2$ and $\mathbf{G}_K\mathbf{K}_{FO} = \mathbf{G}_K\mathbf{W}_1\mathbf{K}_{n\infty}^{FO}\mathbf{W}_2$.

that are related to the load factor output $\breve{\boldsymbol{n}}_{\mathrm{zy},\varepsilon}(s)$ (green in Fig. 22a), the angular rate output $\breve{\boldsymbol{\omega}}_{qr,\varepsilon}(s)$ (green in Fig. 22b), the control signal $\boldsymbol{\delta}_{\mathrm{mn,c},\varepsilon}(s)$ (green in Fig. 22c), and the control signal derivative $\dot{\boldsymbol{\delta}}_{\mathrm{mn,c},\varepsilon}(s)$ (green in Fig. 22d). The sufficiently large reference step amplitudes used on the pitch and yaw-axes are coherent with nonlinear simulations. In Fig. 22a, the pitch/yaw-channel load factor-related responses match the target system responses (red), and hence the time performance in terms of reference tracking (solid lines) and load factor output decoupling (dashed lines) obtained before robust stabilization (black) is very well recovered using the 2DoF RO structure for the robustifying controller, as with the robustifying 2DoF FO controller (magenta). The use of a robustifying 1DoF RO controller is clearly not satisfactory (blue). In Fig. 22b, the output angular rates used for feedback remain small and help to enhance closed loop damping. In Figs. 22c and 22d, the control signals behave well without any saturation nor fast variations.

Robust Stability Analysis

The pitch/yaw-channel linear controller of Fig. 21 is tested for robust stability at the critical operating condition with respect to the projectile dynamics aerodynamic parametric uncertainties, as well as the unstructured uncertainties representing neglected dynamics in the actuator and sensor models. As for the nose position autopilot design, robustness is first assessed using the criterion of the $\mathcal{H}_\infty$ loop-shaping design procedure. The estimated size $\varepsilon = 0.3424$ of NLCF perturbations corresponding to all of the aforementioned modeling uncertainties remains smaller than the stability margin $\varepsilon_{\mathrm{RO2}} = 0.5685$, and hence robust stability is guaranteed.

The μ-analysis theory presented in Subsection "Robust Stability Analysis" of the previous Section "Roll-Channel Autopilot" is also applied to the uncertain pitch/yaw-channel linear closed-loop system, in which the aerodynamic parametric uncertainty block $\boldsymbol{\Delta}_{n\omega}$ similar to Eq. (35), along with the unstructured actuator $\boldsymbol{\Delta}_{\delta}(s)$ and sensor $\boldsymbol{\Delta}_{n,\mathrm{m}}(s), \boldsymbol{\Delta}_{\omega,\mathrm{m}}(s)$ perturbation blocks, are regrouped in a single block-diagonal $\boldsymbol{\Delta}(s) = \mathrm{diag}[\boldsymbol{\Delta}_{\delta}(s), \boldsymbol{\Delta}_{n\omega}, \boldsymbol{\Delta}_{n,\mathrm{m}}(s), \boldsymbol{\Delta}_{\omega,\mathrm{m}}(s)] \in \mathbb{R}\mathcal{H}_\infty, \left\|\boldsymbol{\Delta}(s)\right\|_\infty \leq 1$. Figure 23 gives the upper and lower SSV bounds calculated over a frequency grid, which remain smaller than one and thus indicate robust stability with a good stability margin.

Figures 24a-24f present pitch/yaw load factor, actuator angle and rate time responses for 200 uncertain closed-loop system random samples, using pulse signals of constant amplitude for the reference pitch/yaw-channel load factors. Robust stability of the closed-loop system can be verified, and performance in terms of reference tracking and load factor output decoupling is relatively well ensured, with no canard actuator saturation despite the various sources of modeling uncertainty.

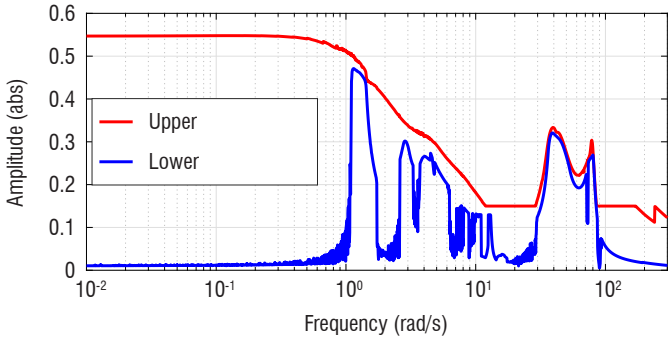

Figure 23 – Upper and lower SSV bounds calculated for the uncertain closed-loop system

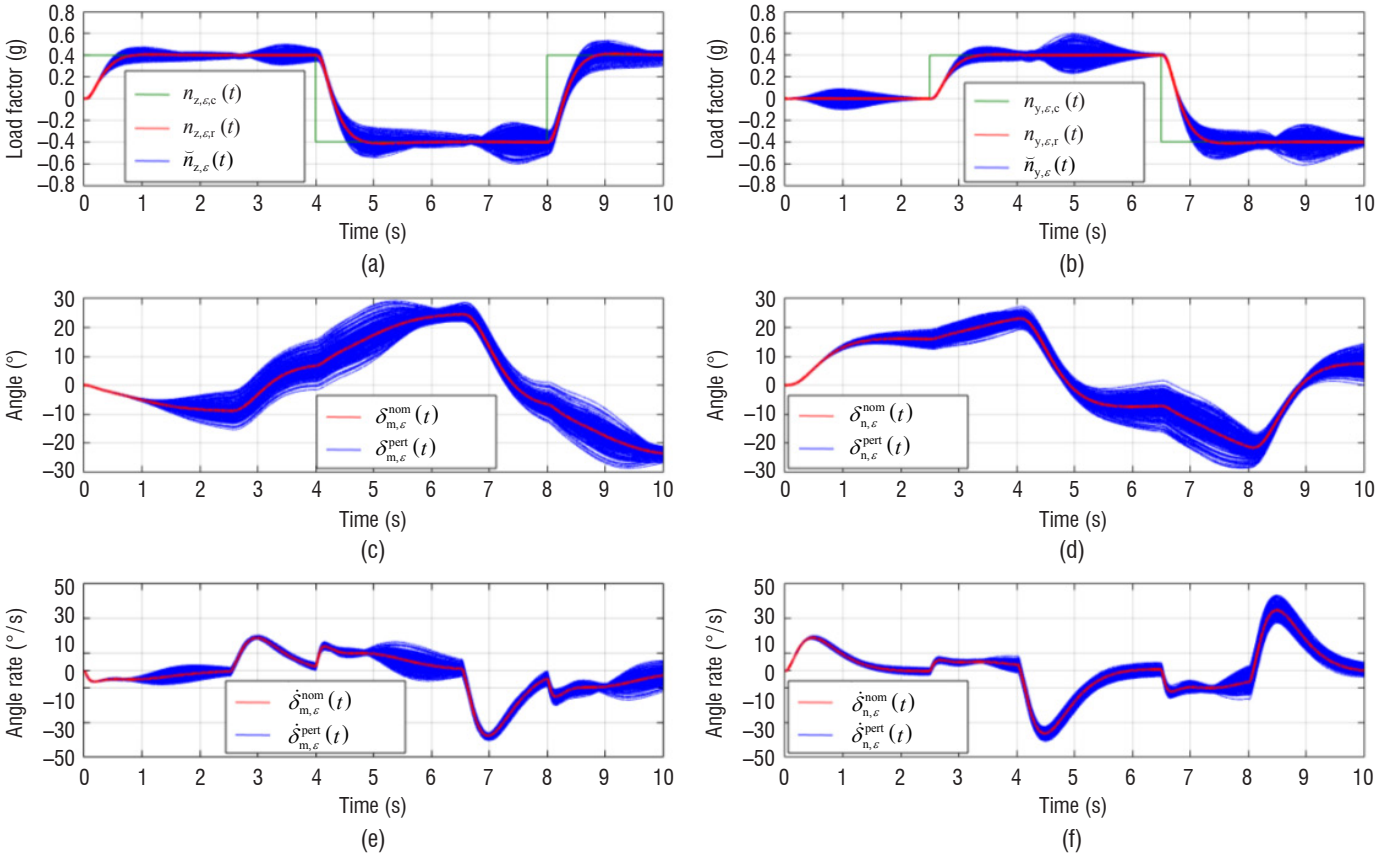

Figure 24 – Uncertain closed-loop simulations: (a) pitch load factor, (b) yaw load factor, (c) pitch actuator angle, (d) yaw actuator angle, (e) pitch actuator angle rate, (f) yaw actuator angle rate

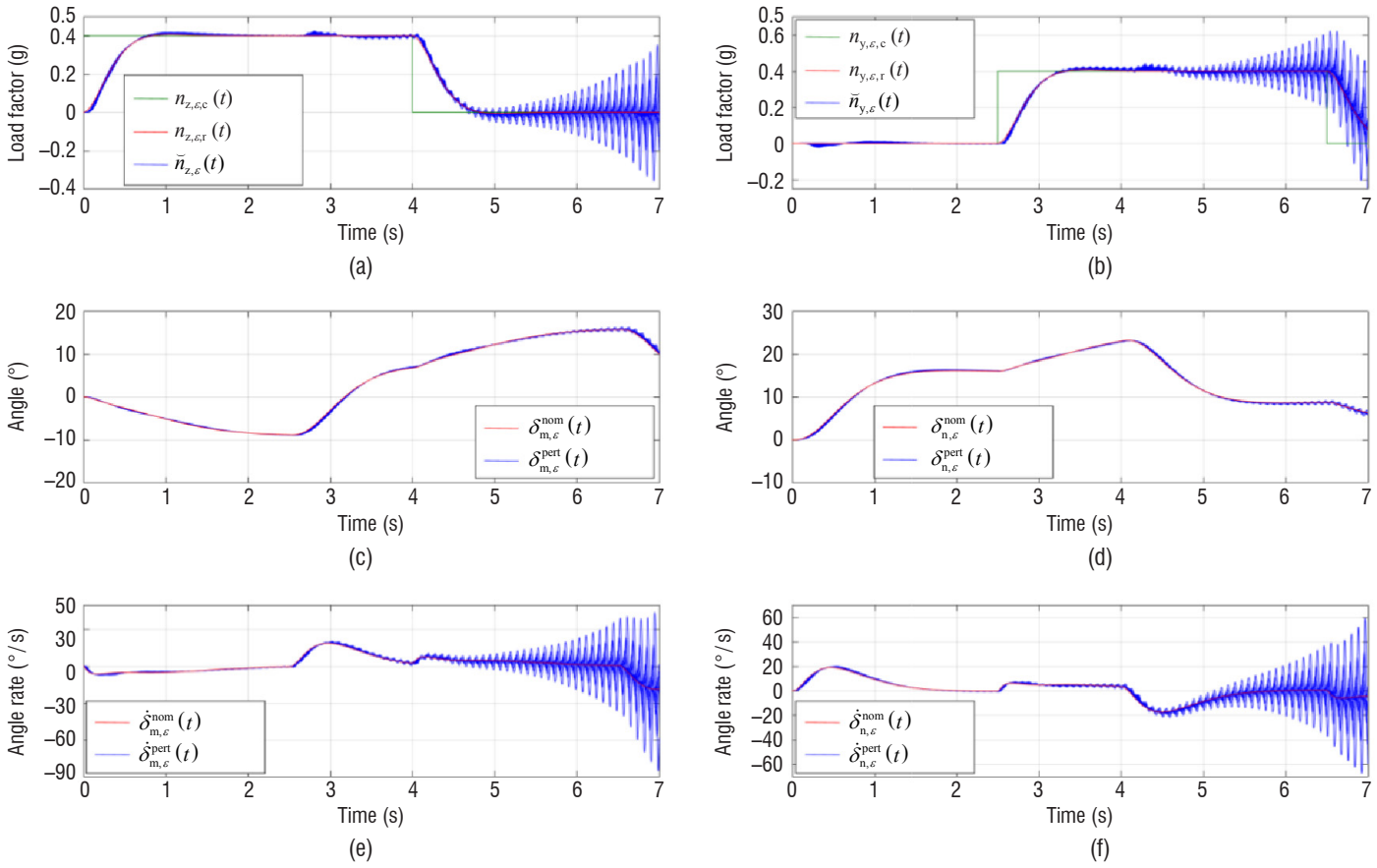

Figure 25 – Closed-loop time responses with transmission delays at actuator inputs: (a) pitch load factor, (b) yaw load factor, (c) pitch actuator angle, (d) yaw actuator angle, (e) pitch actuator angle rate, (f) yaw actuator angle rate

Finally, robust stability of the closed-loop system is verified with respect to transmission delays injected simultaneously at each canard actuator input. For delays of up to 30 ms, *i.e.*, 18 times a rate of 1/600 s with which the control signal could be sampled, Figs. 25a-25f show degradations, on the different time responses considered, which become significant only for the biggest delays. However, for realistic delays of up to 3 times the control signal sampling rate [32], *i.e.*, 5 ms, closed-loop system stability and performance properties are well maintained.

Gain-Scheduled Nonlinear Controller

The development of a gain-scheduled nonlinear controller valid for the entire operating domain $\boldsymbol{\Gamma}_{\mathrm{PY}}^{\lambda}$ of the projectile parameter-dependent pitch/yaw-channel dynamics permits the designer to suitably adapt the control signal level to changes occurring in these dynamics, contrary to a single linear controller, which would be insufficiently robust to ensure desired stability and performance properties for all operating points. Linearly interpolating the eight tuned parameters of a set of controllers, each of which possesses the same structure of Fig. 21 computed by repeating the design procedure of the previous subsections over a grid of equidistant synthesis points covering the trimming envelope $\boldsymbol{\Gamma}_{\mathrm{PY}}^{\lambda}$, produces, for the simplified *q*-LPV model $\mathcal{S}_{\mathrm{PY}}^{\lambda}(\boldsymbol{\lambda}_{\mathrm{PY}})$ of Subsection "Pitch/Yaw-Channels" in Part "Airframe Modeling", a gain-scheduled controller [18]. Implementing directly its structure with the projectile pitch/yaw-channel nonlinear dynamics provides the gain-scheduled *nonlinear* controller of Eq. (46) in which, *i.e.*, $\mathbf{K}_{\omega}^{\lambda} = \mathbf{K}_{\omega}[\boldsymbol{\lambda}_{\mathrm{PY}}(t)]$. The time-dependent scheduling vector $\boldsymbol{\lambda}_{\mathrm{PY}}(t) = [V(t) \;\; h(t)]^{\mathrm{T}}$ is assumed to be measurable as well as slowly-varying for preserving closed-loop system stability. The actuator commands $\boldsymbol{\delta}_{\mathrm{mn,c}}(s)$ are computed again using Eq. (6).

The transformation system $\mathbf{T}_{n\omega}^{\rho}(s, \boldsymbol{\rho}_{\mathrm{PY}})$ of Eqs. (39) is also directly implemented with the nonlinear system dynamics in order to compute for any operating point the necessary feedback signals at the projectile CM, depending on the simultaneously controlled nose angle and rate. The various parameters of the derivative $\mathbf{W}_{\mathrm{d},\omega}(s, \boldsymbol{\lambda}_{\mathrm{PY}})$ and low-pass $\mathbf{W}_{\mathrm{b},n}(s, \boldsymbol{\lambda}_{\mathrm{PY}})$ and $\mathbf{W}_{\mathrm{b},\omega}(s, \boldsymbol{\lambda}_{\mathrm{PY}})$ filters are linearly interpolated using the selected values for the design point grid.

The design of 1886 linear controllers is performed for the same target performance level demanded throughout the entire operating domain. Both the derivative and low-pass filters contained in the transformation system and the model-matching and control signal weighting filters included in the linear controller design setup of Fig. 3 used for open-loop shaping are automatically and smoothly adapted. The PI-P-P controller gain surfaces obtained as a function of the projectile

$$\boldsymbol{\delta}_{\mathrm{zy,c}}(s) = \mathbf{K}_{\delta}(s)\left[\mathbf{K}_{ne}^{\lambda}(s)\left\{\mathbf{K}_{nf}^{\lambda}(s) + \mathbf{K}_{n\infty}^{\lambda}\right\}\mathbf{K}_{\mathrm{nsc}}^{\lambda} \;\middle|\; -\left\{\mathbf{K}_{ne}^{\lambda}(s)\mathbf{K}_{n\infty}^{\lambda} + \mathbf{K}_{nn}^{\lambda}\right\} \;\; -\mathbf{K}_{\omega}^{\lambda}\right]\begin{bmatrix} \boldsymbol{n}_{\mathrm{zy,c}}(s) \\ \breve{\boldsymbol{n}}_{\mathrm{zy}}(s) \\ \breve{\boldsymbol{\omega}}_{qr}(s) \end{bmatrix} \tag{46}$$

airspeed V and altitude h are given in Figs. 26, 27, whereas the values of the different parameters of the pre-filter and of the robustifying 2DoF $\mathcal{H}_\infty$ controller, which remain almost constant over the flight envelope, are not shown for brevity purposes. The reasonable values of the PI-P-P controller gains vary relatively smoothly[3], hence aiding the obtainment of a good continuity of the gain-scheduled control signal during transitions between synthesis operating points, which is desirable for preserving the performance and robustness properties [19, 27].

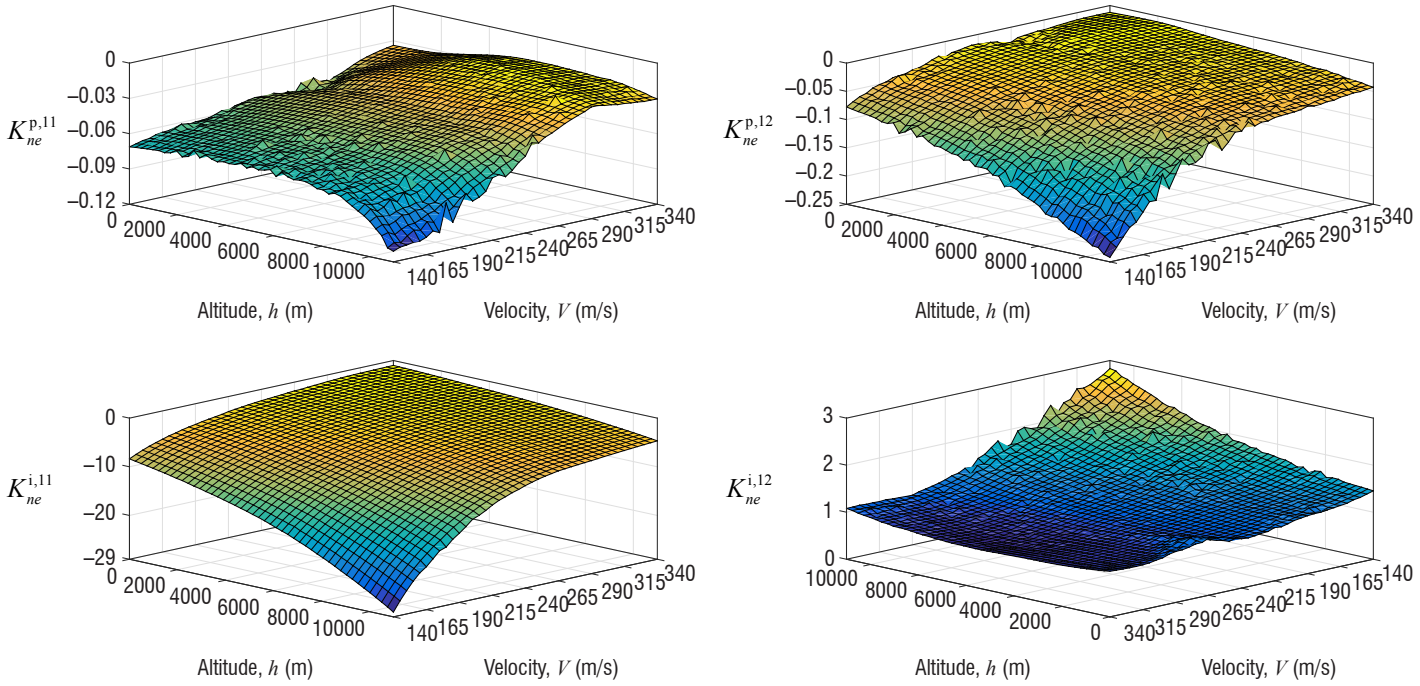

Figure 26 – Gain surfaces as a function of the synthesis point for controller $\mathbf{K}_{ne}(s,\overline{\boldsymbol{\lambda}}_{\mathrm{PY}})$

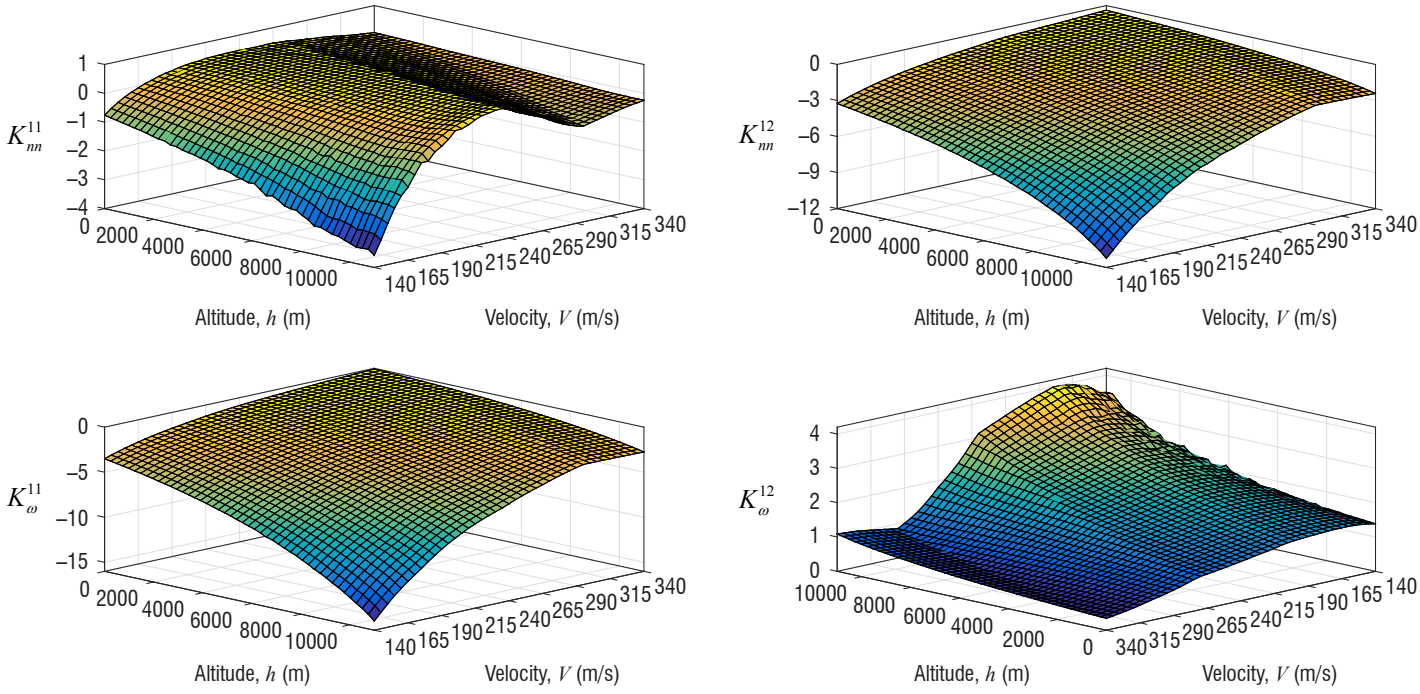

Figure 27 – Gain surfaces as a function of the synthesis point for controllers $\mathbf{K}_{nn}(\overline{\boldsymbol{\lambda}}_{\mathrm{PY}}),\mathbf{K}_{\omega}(\overline{\boldsymbol{\lambda}}_{\mathrm{PY}})$

[3] Whereas the proposed controller design procedure provides gain surfaces which are already relatively smooth, a subsequent smoothing could be applied to the gains in order to obtain smoother variations.

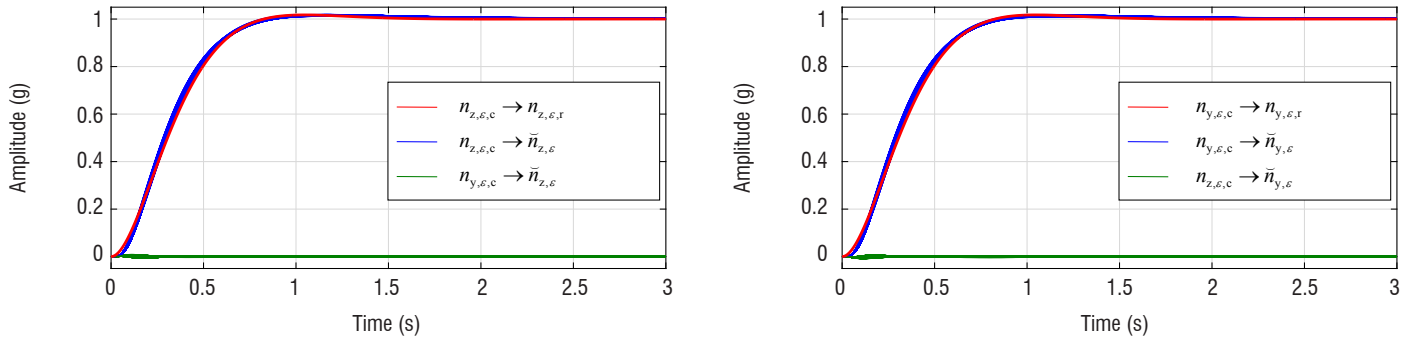

Figure 28 – Closed-loop load factor step responses for all design points: (a) pitch-axis, (b) yaw-axis

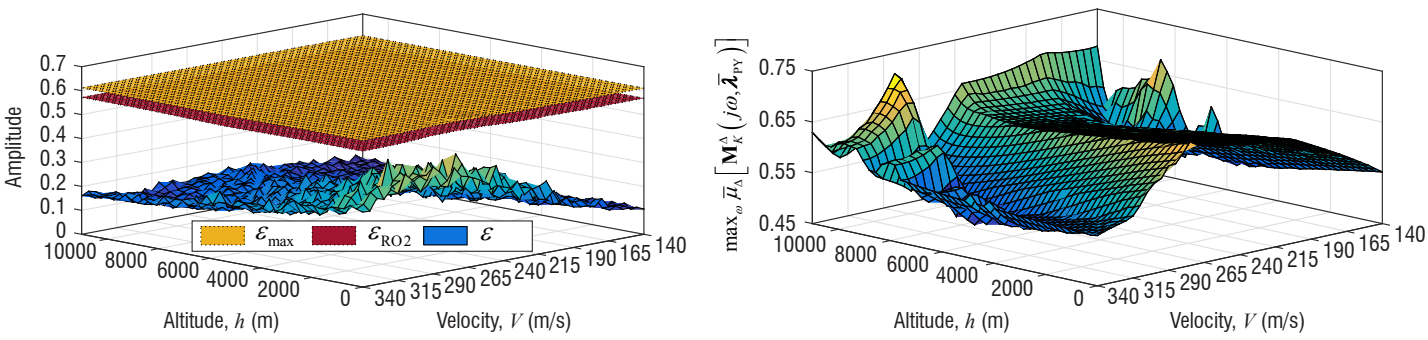

Figure 29 – Robustness results as a function of the synthesis point: (a) maximal $\varepsilon_{\max}(\bar{\boldsymbol{\lambda}}_{PY})$ (yellow) and achieved $\varepsilon_{RO2}(\bar{\boldsymbol{\lambda}}_{PY})$ (red) NLCF stability margins along with uncertainty size $\varepsilon(\bar{\boldsymbol{\lambda}}_{PY})$ (blue), (b) maximal value over frequency of the SSV upper bound

Figures 28a, 28b illustrate for all synthesis points the closed-loop pitch/yaw load factor output-related step responses (blue, green) indicating that the reference tracking and output decoupling local performance objectives specified by the reference dynamics (red) are very well met over the trimming envelope. Figures 29a, 29b indicate that closed-loop system local robust stability is proved at each design point using both the robustness criterion of the $\mathcal{H}_\infty$ loop-shaping design procedure and μ-analysis theory. For the considered modeling uncertainty, the inequalities $\varepsilon(\bar{\boldsymbol{\lambda}}_{PY}) < \varepsilon_{RO2}(\bar{\boldsymbol{\lambda}}_{PY})$ and $\max_{\omega} \bar{\mu}_{\Delta}[\mathbf{M}_K^{\Delta}(j\omega, \bar{\boldsymbol{\lambda}}_{PY})] < 1, \forall \omega \in \mathbb{R}^+$ are verified for any synthesis point $\bar{\boldsymbol{\lambda}}_{PY} \in \boldsymbol{\Gamma}_{PY}^{\lambda}$.

The nonlocal stability and performance properties provided by the gain-scheduled controller are now verified using the simplified q-LPV model $\mathcal{S}_{PY}^{\lambda}(\boldsymbol{\lambda}_{PY})$ proposed in Subsection "Pitch/Yaw-Channels" of Part "Airframe Modeling". The latter is simulated during 28 s along a parameter vector test trajectory $\boldsymbol{\lambda}_{PY}(t)$ covering the flight envelope $\boldsymbol{\Gamma}_{PY}^{\lambda}$, as shown in Fig. 30. The altitude trajectory originates from a ballistic simulation of 28 s between the apogee and the impact point, whereas the airspeed is a chirp sinusoidal signal whose frequency increases from 0.01 Hz to 0.1 Hz at a linear rate with time during 15 s and then at the same rate up to 28 s. The simulation time results obtained with reference pitch/yaw load factors taken as pulse signals of constant amplitude are presented in Figs. 31a-31d. Performance in terms of reference tracking and decoupling is satisfactory and the pitch and yaw actuator angular position and rate signals behave well.

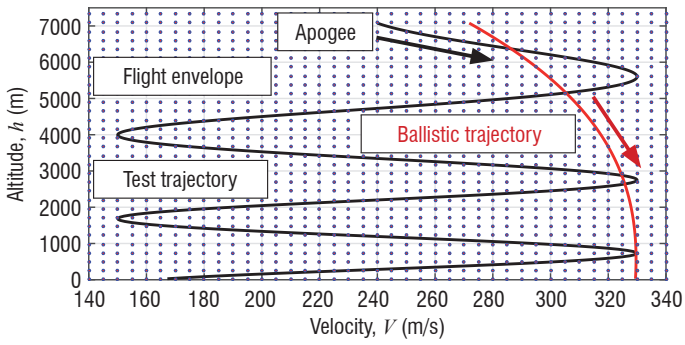

Figure 30 – Evolution of the scheduling vector test trajectory within the projectile flight envelope covered by the equidistant synthesis point grid (black: test trajectory, red: ballistic trajectory)

Proportional Navigation Guidance Algorithm

This part describes the gravity-compensation *pure* proportional navigation (PPN) guidance algorithm, which generates the suitable reference pitch/yaw-channel load factor orders commanded to the autopilot in order to steer with accuracy the projectile to a given target. The load factor commands expressed in the non-rolling frame CS are given by [40]:

$$\left[\boldsymbol{n}_c^{BE}\right]^{B'} = \frac{N\left[\boldsymbol{\omega}^{OE}\right]^{B'} \times \left[\boldsymbol{v}_B^E\right]^{B'} - \left[\mathbf{T}\right]^{B'E}\left[\boldsymbol{g}\right]^E}{\left\|\left[\boldsymbol{g}\right]^E\right\|} \tag{47}$$

The vector $[\boldsymbol{\omega}^{OE}]^{B'}$ is the line of sight O rate of change with respect to the inertial frame E and is defined as:

$$\left[\boldsymbol{\omega}^{OE}\right]^{B'} = \left[\mathbf{T}\right]^{B'E} \frac{\left[\boldsymbol{s}_{TB}\right]^E \times \left[\boldsymbol{v}_{TB}^E\right]^E}{\left\|\left[\boldsymbol{s}_{TB}\right]^E\right\|^2} \tag{48}$$

where the line of sight vector $[\boldsymbol{s}_{TB}]^E = [\boldsymbol{s}_{TE}]^E - [\boldsymbol{s}_{BE}]^E$ is the differential inertial position vector between the projectile CM B and the target

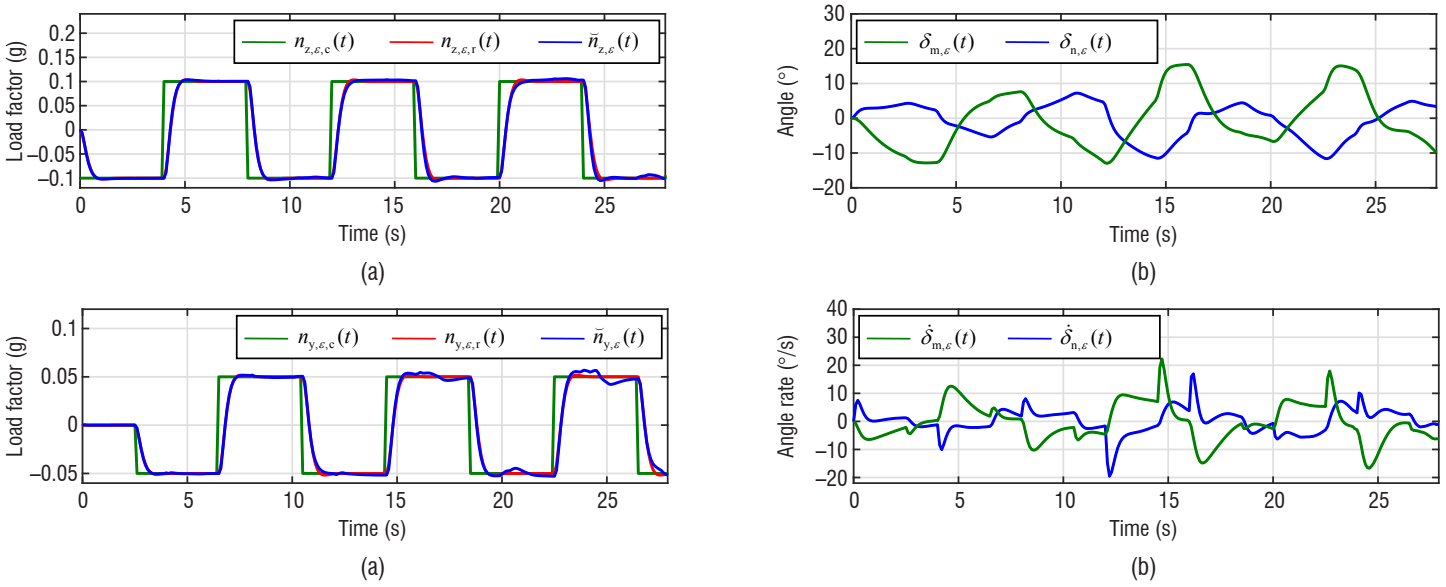

Figure 31 – Closed-loop simulations: (a) pitch load factor, (b) yaw load factor, (c) pitch/yaw actuator angles, (d) pitch/yaw actuator angular rates

CM T positions, which are considered as perfectly known, and the differential velocity vector $[\boldsymbol{v}_{\mathrm{TB}}^{\mathrm{E}}]^{\mathrm{E}} = [\boldsymbol{v}_{\mathrm{T}}^{\mathrm{E}}]^{\mathrm{E}} - [\boldsymbol{v}_{\mathrm{B}}^{\mathrm{E}}]^{\mathrm{E}}$ of the projectile CM B with respect to the target frame T is the difference between the inertial projectile and target velocity vectors.

The PPN constant is here set to $N = 2.5$, since this value leads to reasonable amplitudes for the reference load factors, and to smaller, slower-varying and more homogenous over time amplitudes for the canard actuator control signals. Hence, the risk of actuator saturation is limited, while a very good impact accuracy is maintained.

The gravitational acceleration vector is given by $[\boldsymbol{g}]^{\mathrm{E}} = [0 \;\; 0 \;\; g]^{\mathrm{T}}$ in the inertial CS and it is expressed in the non-rolling frame CS using the transformation matrix $[\mathbf{T}]^{\mathrm{B'E}}$, which is defined as follows as a function of the projectile pitch and yaw Euler angles assumed as perfectly known:

$$[\mathbf{T}]^{\mathrm{B'E}} = \begin{bmatrix} \cos\theta\cos\psi & \cos\theta\sin\psi & -\sin\theta \\ -\sin\psi & \cos\psi & 0 \\ \sin\theta\cos\psi & \sin\theta\sin\psi & \cos\theta \end{bmatrix} \tag{49}$$

There exists an alternative *true* PN (TPN) guidance law [39, 40] which possesses a similar expression to that of the PPN law. The difference comes from the use in Eq. (47) of the differential velocity vector expressed in the non-rolling frame CS $[\boldsymbol{v}_{\mathrm{TB}}^{\mathrm{E}}]^{\mathrm{B'}}$ instead of the projectile CM velocity vector $[\boldsymbol{v}_{\mathrm{B}}^{\mathrm{E}}]^{\mathrm{B'}}$. A PPN guidance law generates a commanded load factor vector that is normal to the inertial velocity vector $[\boldsymbol{v}_{\mathrm{B}}^{\mathrm{E}}]^{\mathrm{E}}$, whereas a TPN guidance law orders a load factor vector normal to the line of sight, *i.e.*, normal to the differential inertial velocity vector $[\boldsymbol{v}_{\mathrm{TB}}^{\mathrm{E}}]^{\mathrm{E}}$. However, both PPN and TPN laws yield identical commanded load factors in the case of a non-maneuvering target.

Nonlinear Simulation Results

This part proves the effectiveness of the guidance & gain-scheduled nonlinear control (G&C) system designed for an STT canard-guided dual-spin projectile, when it is implemented with the complete 7DoF nonlinear model of Part "Airframe Modeling" augmented with the transformation system, throughout various simulation scenarios of a complete guided flight. Such a guided flight here comprises two main phases: the *ballistic* phase (from launch to a few seconds after the projectile trajectory apogee) and the *guided* phase (from the end of the ballistic phase to the projectile impact).

The ballistic phase $(0 \le t < t_{\mathrm{guid}})$, where no guidance function is engaged, starts at projectile launch with a muzzle velocity $V_0 = 803$ m/s, and gun barrel pointing $\theta_0 \simeq 899.9$ mil $= 50.62°$ and azimuth $\psi_0 \simeq +2026.7$ mil $= +114°$ (south-easterly direction). The ballistic phase comprises three subphases: a first *starting* subphase $(0 \le t < t_{\mathrm{start}} = 20\,\mathrm{s})$, a second *nose rate reduction* subphase $(t_{\mathrm{start}} = 20\,\mathrm{s} \le t < t_{\mathrm{switch}} = 40\,\mathrm{s})$, and a third *nose position reset* subphase $(t_{\mathrm{switch}} = 40\,\mathrm{s} \le t < t_{\mathrm{guid}})$. During the first subphase, the nose embedded electronic components (G&C modules, actuators and sensors) are started only a few seconds after launch, in order to avoid their potential degradation caused by the extreme launch accelerations. Large disturbances appearing in different system signals are also sufficiently reduced during this first subphase. During the second subphase, the high roll rate of the nose initially fixed with the projectile body is reduced to zero using the rate autopilot. During the third subphase, the nose angle is reset to $\phi_{\mathrm{f}} = 180°$ by the position autopilot and the steering canards are deployed at $t_{\mathrm{eng}} = 40.5\,\mathrm{s}$.

The guided phase $(t_{\mathrm{guid}} \le t \le t_{\mathrm{impact}})$ starts after the trajectory apogee, when the projectile arrives at less than 10 km from the target. With the projectile maneuvering with an STT mode for trajectory correction, the nose angle is permanently regulated about $\phi_{\mathrm{f}} = 180°$ from t_{guid}. The pitch/yaw-channel PPN guidance function, which is however engaged only as from $t_{\mathrm{guid}} + 3\,\mathrm{s}$ when the large disturbances on the feedback signals due to canard deployment are sufficiently reduced, actively directs the projectile with accuracy towards a ballistic impact point.

Nonlinear simulation results are given in Figs. 32 and 33, considering nominal initial conditions (IC), no wind and no modeling uncertainty. Figures 32a-32f illustrate on the left for the pitch/yaw-channels the tracking load factors and the canard actuator deflection angles and rates, whereas on the right the nose roll-channel controlled angle, the angular rate and the input voltage to the coaxial motor are given. Figures 33a-33b show the aerodynamic angles AoA and AoS and their derivatives with respect to time. During the ballistic phase $(0 \le t \lesssim 49\,\mathrm{s})$, the nose roll rate is correctly reduced to zero from

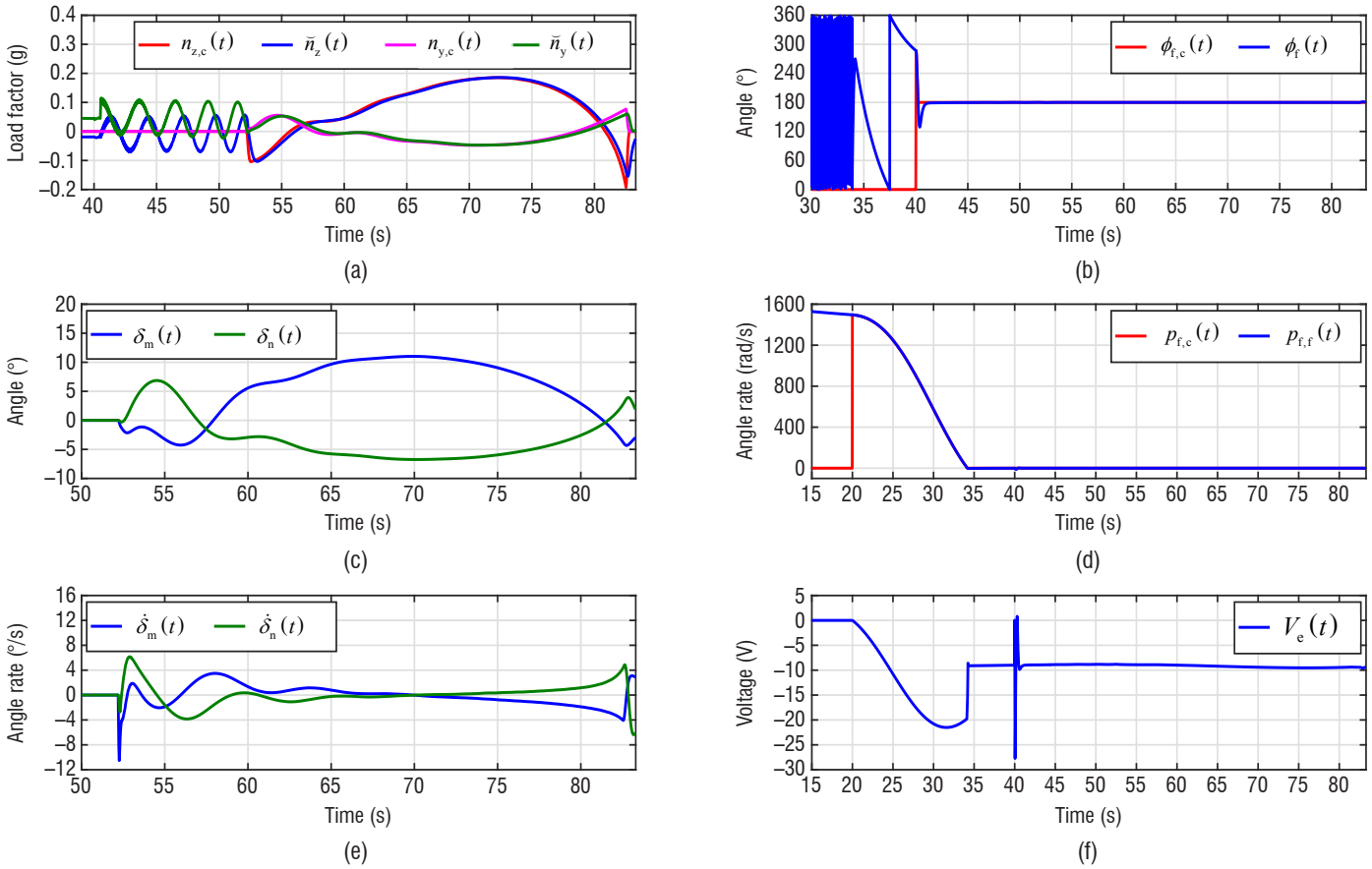

Figure 32 – Nominal scenario: (a) pitch/yaw load factors, (b) nose angle, (c) pitch/yaw actuator angles, (d) nose angle rate, (e) pitch/yaw actuator angle rates, (f) actuator voltage

$t_{start} = 20$ s (Fig. 32d), and the nose angle is then well reset to the position $\phi_f = 180°$ from $t_{switch} = 40$ s (Fig. 32a), despite the disturbances of Eq. (14) appearing in the nose position and rate dynamics. In addition, the voltage applied to the coaxial motor never exceeds the saturation value $V_{e,sat} = 60$ V and behaves almost always smoothly (Fig. 32f), hence aiding in saving energy.

During the guided phase ($49 \text{ s} \lesssim t \lesssim 83$ s), the nose position autopilot keeps on performing well (Figs. 32b, 32f) and does not inject any perceptible lag into the controlled pitch/yaw-channels, for which the commanded load factor tracking starting at $t \simeq 52$ s is excellent even for fast reference load factors sent by the PPN guidance loop at the end of the flight (Fig. 32a). The ballistic impact accuracy for a range of more than 20 km is very good, using here a perfect navigation, as the range and crossrange errors are both smaller than 25 cm.

The STT projectile globally maneuvers more in the vertical plane rather than in the horizontal plane, as shown in Figs. 32c and 32e, where the pitch canard actuator is the most solicited. However, the canard actuator deflection angles and rates remain all the time quite far from the saturation limits $\delta_{sat} = \pm 30°$ and $\dot{\delta}_{sat} = \pm 100°/s$.

The large disturbances caused on the load factor output signals by canard deployment at $t_{eng} = 40.5$ s are well rejected. The gain-scheduled nonlinear controller also provides a very good nonlocal performance, although the aerodynamic angles illustrated in Fig. 33a take values more or less far from the zero values imposed in the trimming vector for computing the set of linear controllers. Hence, the obtained performance is robust with respect to the resulting uncertainty on the trimming vector. In addition, performance is well maintained even though the pitch/yaw-channel dynamics system does not actually operate at equilibrium, as seen from the non-zero values of $\dot{\alpha}, \dot{\beta}$ given in Fig. 33b.

Three additional nonlinear simulation scenarios are finally addressed. The first scenario considers uncertainty on the launch IC's through errors placed on the muzzle velocity V_0 and on the gun barrel pointing θ_0 and azimuth ψ_0. The second scenario studies the capability of the autopilot to reject wind disturbances. The third scenario

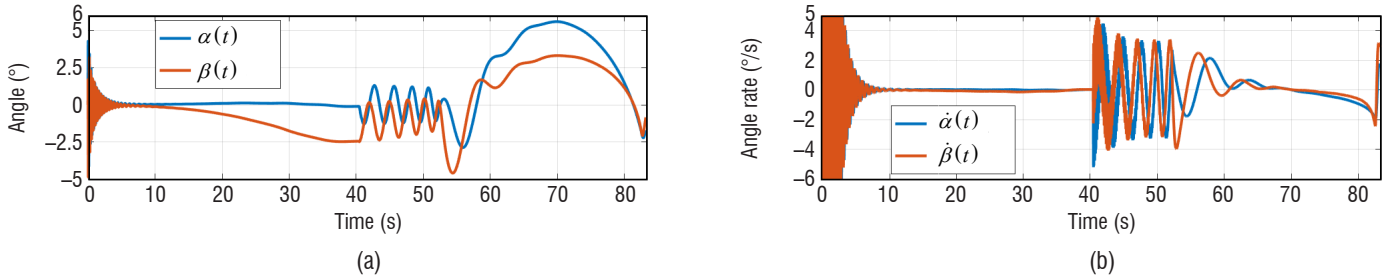

Figure 33 – Nominal closed-loop simulations: (a) AoA and AoS, (b) AoA and AoS time derivatives

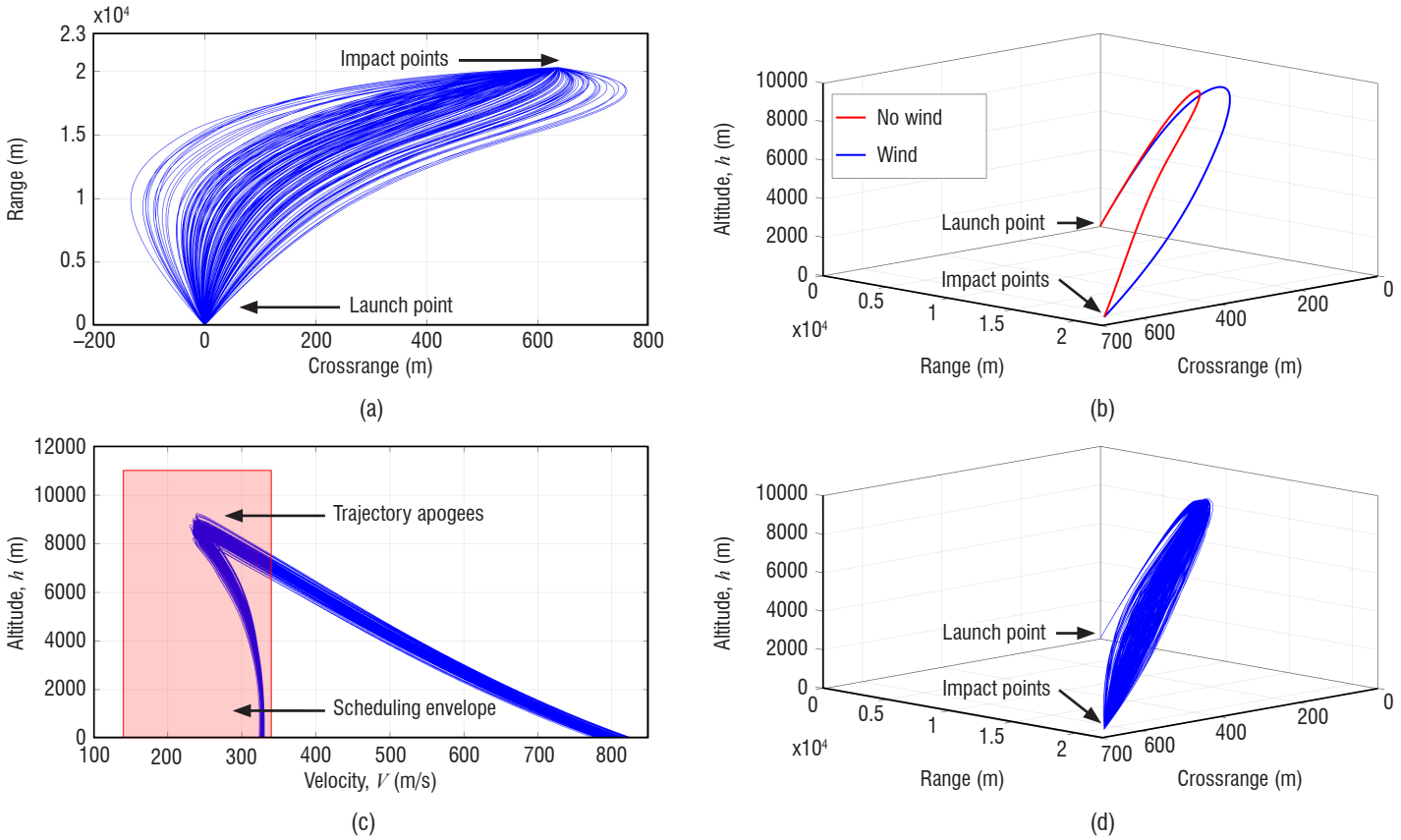

Figure 34 – Nonlinear scenarios: (a) & (c) uncertain IC's, (b) wind disturbances, (d) aerodynamic and component uncertainties

evaluates the robustness to the uncertainty modeled in the projectile aerodynamic coefficients and in the actuator and sensor dynamics (see Part "Airframe Modeling").

Concerning the first scenario, 200 random cases are simulated, in which the variables V, θ, ψ are independent, normally distributed, random numbers with a mean value equal to their nominal values $V_0 = 803$ m/s, $\theta \simeq 899.9$ mil, $\psi_0 \simeq +2026.7$ mil and a standard deviation of 10 m/s for V and of $0.5° \simeq 8.9$ mil for θ,ψ. Figure 34a illustrates the top view of the various projectile trajectories, where it can be seen that the designed G&C system performs well to always direct the projectile to the target with good precision and accuracy. Figure 34c gives the trajectories for the pitch/yaw-channel controller scheduling vector $\boldsymbol{\lambda}_{\text{PY}} = [V \;\; h]^{\text{T}}$. For the flight conditions corresponding to the projectile guided phase, all of the trajectories belong to the controller scheduling envelope $\boldsymbol{\Gamma}^{\boldsymbol{\lambda}}_{\text{PY}}$.

Concerning the second scenario, the MATLAB/Simulink `Horizontal Wind Model 07` is used for a latitude of 47.1° north, longitude of 2.4° east and altitude covering the interval [0.12000m], at 1 a.m. UTC of October 2nd 2015, using an Ap index of 48. As seen from the 3D projectile trajectories given in Fig. 34b, even though the wind leads to significantly modifying the projectile trajectory compared to the no-wind case, the wind disturbances are very well rejected by the autopilot and the projectile hits the target.

Concerning the third scenario, 300 trajectories are simulated using for each of them independent, uniformly distributed, random values for the 16 aerodynamic coefficients and the 5 coaxial motor parameters, along with random perturbed systems for the pitch/yaw-channel actuator and sensor uncertain models. Figure 34d shows that closed-loop system robust stability is ensured and that the guidance commands are successfully followed, permitting the projectile to hit the target in each case.

Concluding Remarks

This paper deals with the development of guidance and control functions for the roll, pitch and yaw-channels of a 155 mm Skid-To-Turn canard-guided spin-stabilized projectile. The complete 7DoF nonlinear and subsequently derived linearized models are addressed, and those consider the actual nose-mounted sensor position for modeling realism improvement. The application of an $\mathcal{H}_\infty$ loop-shaping design approach provides a linear autopilot for the nose roll-channel, along with a gain-scheduled controller for the complete airframe pitch/yaw-channels. Both separately designed autopilots offer high performance and robustness linear properties despite their quite simple fixed and reduced order structures. The proposed pure proportional navigation guidance and gain-scheduled control scheme is proved to be very efficient for hitting a ballistic target with a high level of precision and accuracy, through various guided flight scenarios considering nominal, perturbed or uncertain nonlinear operating conditions.

Future works for autopilot design could focus on developing an anti-windup control scheme for handling potential actuator amplitude and rate saturations. Alternative controller interpolation laws, theoretically guaranteeing global closed-loop system stability, contrary to the linear interpolation technique used here, could also be studied. In addition, it would be interesting to design a purely LPV controller and compare it to the gain-scheduled autopilot proposed here ■

Aknowledgment

The authors would like to thank the French Ministry of Defence Procurement Agency (*Direction Générale de l'Armement – DGA*) for financial support.

References

[1] P. APKARIAN, D. NOLL - *Nonsmooth $\mathcal{H}_\infty$ Synthesis*. IEEE Transactions on Automatic Control, 51(1), p. 71-86, January 2006.

[2] K. J. ÅSTRÖM - *Limitations on Control System Performance*. European Journal of Control, 6(1), p. 2-20, 2000.

[3] J.-M. BIANNIC, P. APKARIAN - *Missile Autopilot Design via a Modified LPV Synthesis Technique*. Aerospace Science and Technology, 3(3), p. 153-160, April 1999.

[4] J.-D. BLIGHT, R. L. DAILEY, D. GANGSAAS - *Practical Control Law Design for Aircraft using Multivariable Techniques*. International Journal of Control, 59(1), p. 93-137, January 1994.

[5] B. BURCHETT, A. PETERSON, M. COSTELLO - *Prediction of Swerving Motion of a Dual-Spin Projectile with Lateral Pulse Jets in Atmospheric Flight*. Mathematical and Computer Modelling, 35(7-8), p. 821-834, April 2002.

[6] D. CARLUCCI , S. JACOBSON - *Ballistics: Theory and Design of Guns and Ammunition*. CRC Press, 2007.

[7] B. CHOI, S. KANG, H. J. KIM, B.-E. JUN, J.-I. LEE, M.-J. TAHK, C. PARK - *Roll-Pitch-Yaw Integrated μ-Synthesis for High Angle-of-Attack Missiles*. Aerospace Science and Technology, 23(1), p. 270-279, December 2012.

[8] M. COSTELLO, A. PETERSON - *Linear Theory of a Dual-Spin Projectile in Atmospheric Flight*. Journal of Guidance, Control, and Dynamics, 23(5), p. 789-797, September-October 2000.

[9] G. COOPER, F. FRESCONI, M. COSTELLO - *Flight Stability of an Asymmetric Projectile with Activating Canards*. Journal of Spacecraft and Rockets, 49(1), p. 130-135, January-February 2012.

[10] M. A. CREAGH, D. J. MEE - *Attitude Guidance for Spinning Vehicles with Independent Pitch and Yaw Control*. Journal of Guidance, Control, and Dynamics, 33(3), p. 915-922, May-June 2010.

[11] J. C. DOYLE, G. STEIN - *Multivariable Feedback Design: Concepts for a Classical/Modern Synthesis.* IEEE Transactions on Automatic Control, 26(1), p. 4-16, February 1981.

[12] F. FRESCONI - *Guidance and Control of a Projectile with Reduced Sensor and Actuator Requirements*. Journal of Guidance, Control, and Dynamics, 34(6), p. 1757-1766, November-December 2011.

[13] F. FRESCONI, I. CELMINS, S. SILTON, M. COSTELLO - *High Maneuverability Projectile Flight using Low Cost Components*. Aerospace Science and Technology, 41, p. 175-188, February 2015.

[14] D. W. C. HO, J. LAM, T. W. K. CHAN - *An Application of $\mathcal{H}_\infty$ Design to Model-Following.* International Journal of Control, 55(2), p. 483-509, 1992.

[15] J. B. HOAGG, D. S. BERNSTEIN - *Nonminimum-Phase Zeros: Much to Do about Nothing - Classical Control Revisited*. Part II. IEEE Control Systems Magazine, 27(3), p. 45-57, June 2007.

[16] P. B. JACKSON - *Overview of Missile Flight Control Systems.* Johns Hopkins APL Technical Digest, 29(1), p. 9-24, 2010.

[17] P. B. JACKSON - *Robust Control and $\mathcal{H}_\infty$-Optimization-Tutorial Paper.* Automatica, 29(2), p. 255-273, March 1993.

[18] G. A. LAWRENCE, W. J. RUGH - *Gain Scheduling Dynamic Linear Controllers for a Nonlinear Plant.* Automatica, 31(3), p. 381-390, March 1995.

[19] D. J. LEITH, W. E. LEITHEAD - *Survey of Gain-Scheduling Analysis and Design.* International Journal of Control, 73(11), p. 1001-1025, January 2000.

[20] A. MARCOS, G. J. BALAS - *Development of Linear-Parameter-Varying Models for Aircraft.* Journal of Guidance, Control, and Dynamics, 27(2), p. 218-228, March-April 2004.

[21] R. L. McCOY - *Modern Exterior Ballistics: The Launch and Flight Dynamics of Symmetric Projectiles.* Schiffer Publishing, Ltd., 2012.

[22] D. C. McFARLANE, K. GLOVER - *Robust Controller Design Using Normalized Coprime Factor Plant Descriptions.* Springer-Verlag New York, 1990.

[23] D. C. McFARLANE, K. GLOVER - *A Loop-Shaping Design Procedure using $\mathcal{H}_\infty$ Synthesis.* IEEE Transactions on Automatic Control, 37(6), p. 759-769, June 1992.

[24] D. OLLERENSHAW, M. COSTELLO - *Model Predictive Control of a Direct Fire Projectile Equipped With Canards.* Journal of Dynamic Systems, Measurement, and Control, 130(6), p. 61010-1–61010-11, November 2008.

[25] P. C. PELLANDA, P. APKARIAN, H. D. TUAN - *Missile Autopilot Design via a Multi-Channel LFT/LPV Control Method.* International Journal of Robust and Nonlinear Control, 12(1), p. 1-20, January 2002.

[26] J. ROGERS, M. COSTELLO - *Design of a Roll-Stabilized Mortar Projectile with Reciprocating Canards.* Journal of Guidance, Control, and Dynamics, 33(4), p. 1026-1034, July-August 2010.

[27] W. J. RUGH, J. S. SHAMMA - *Research on Gain Scheduling.* Automatica, 36(10), p. 1401-1425, October 2000.

[28] F. SÈVE, S. THEODOULIS, P. WERNERT, M. ZASADZINSKI, M. BOUTAYEB - *Sensor Position Influence on Modeling and Control of 155mm Canard-Guided Spin-Stabilized Projectiles.* IEEE International Conference on Control, Decision and Information Technologies (CoDIT), p. 358-363, Metz, France, November 2014.

[29] J. S. SHAMMA, J. R. CLOUTIER - *Gain-Scheduled Missile Autopilot Design Using Linear Parameter Varying Transformations.* Journal of Guidance, Control, and Dynamics, 16(2), p. 256-263, March-April 1993.

[30] S. SKOGESTAD, I. POSTLETHWAITE - *Multivariable Feedback Control: Analysis and Design.* John Wiley & Sons, Ltd, 2005.

[31] N. SLEGERS - *Predictive Control of a Munition Using Low-Speed Linear Theory.* Journal of Guidance, Control, and Dynamics, 31(3), p. 768-775, May-June 2008.

[32] B. L. STEVENS, F. L. LEWIS - *Aircraft Control and Simulation.* John Wiley & Sons, Inc., 2003.

[33] S. THEODOULIS, V. GASSMANN, P. WERNERT, L. DRITSAS, I. KITSIOS, A. TZES - *Guidance and Control Design for a Class of Spin-Stabilized Fin-Controlled Projectiles.* Journal of Guidance, Control, and Dynamics, 36(2), p. 517-531, March-April 2013.

[34] S. THEODOULIS, F. SÈVE, P. WERNERT - *Robust Gain-Scheduled Autopilot Design for Spin-Stabilized Projectiles with a Course-Correction Fuze.* Aerospace Science and Technology, 42, p. 477-489, April-May 2015.

[35] K. A. WISE - *Bank-to-turn Missile Autopilot Design using Loop Transfer Recovery.* Journal of Guidance, Control, and Dynamics, 13(1), p. 145-152, January-February 1990.
[36] K. A. WISE, D. J. BROY - *Agile Missile Dynamics and Control.* Journal of Guidance, Control, and Dynamics, 21(3), p. 441-449, May-June 1998.
[37] B. A. WHITE, L. BRUYERE, A. TSOURDOS - *Missile Autopilot Design using Quasi-LPV Polynomial Eigenstructure Assignment.* IEEE Transactions on Aerospace and Electronic Systems, 43(4), p. 1470-1483, October 2007.
[38] R. YANUSHEVSKY - *Modern Missile Guidance.* CRC Press, 2008.
[39] P. ZARCHAN - *Tactical and Strategic Missile Guidance.* American Institute of Aeronautics and Astronautics, Inc., 2012.
[40] P. H. ZIPFEL - *Modeling and Simulation of Aerospace Vehicle Dynamics.* American Institute of Aeronautics and Astronautics, Inc., 2014.
[41] K. ZHOU, J. C. DOYLE, K. GLOVER - *Robust and Optimal Control.* Prentice-Hall, Inc., 1996.

Acronyms

CNRS	(Centre National de la Recherche Scientifique - *National Center for Scientific Research*)
CRAN	(Centre de Recherche en Automatique de Nancy - *Research Center for Automatic Control of Nancy*)
DGA	(Direction Générale de l'Armement - *French Ministry of Defence Procurement Agency*)
ISL	(Institut Franco-Allemand de Recherches de Saint-Louis - *French-German Research Institute of Saint-Louis*)

AUTHORS

Florian Sève received the Engineering degree in automatic control engineering from Télécom Physique Strasbourg, Strasbourg, France, in 2011, and the M.Sc. degree in automatic control and robotics from the University of Strasbourg, Strasbourg, France, in 2011. Since 2011, he had been a Ph.D. student at both the French-German Research Institute of Saint-Louis (ISL), Saint-Louis, France, and the University of Lorraine, Longwy, France, and in 2016, he received the Ph.D. degree in automatic control engineering from the University of Lorraine, France. During 2014-2015, he was a Research Assistant and a Teaching Assistant at the University of Lorraine. Since 2016, he has been a Research Associate in the Department of Guidance, Navigation and Control, French-German Research Institute of Saint-Louis. His research interests include flight dynamics modeling and development of control and guidance algorithms for guided ammunition.

Spilios Theodoulis received the diploma degree in Electrical Engineering from the University of Patras, Patras, Greece, in 2004, the M.Sc. in systems and control from Université Paul Sabatier, Toulouse, France, in 2005, and the Ph.D. degree in control systems from Université Paris Sud, Orsay, France, in 2008. Since 2009, he has been a tenured Researcher in the Department of Guidance, Navigation and Control, French-German Research Institute of Saint-Louis (ISL), Saint-Louis, France. His research interests include flight dynamics and control as well as system and hardware in the loop simulation for guided ammunition and UAV's.

Philippe Wernert studied aeronautics engineering at Ecole Nationale Supérieure de Méchanique et d'Aérotechnique (ENSMA Poitiers in France) and received the *Diplôme d'Ingénieur* in 1989. He joined the French-German Research Institute of Saint-Louis (ISL) in 1990 and graduated (Ph.D. summa cum laude) with University of Marseille (France) in 1997. From 1990 to 2000, he was mainly involved in the development and application of measuring techniques for the study of projectiles aerodynamics in subsonic and supersonic wind tunnels. Since 2000, he is in charge of the study, development and expertise of existing or new concepts of guided flying vehicles (mainly gun launched guided projectiles and microdrones). To this purpose, he developed specific trajectory and system analysis simulation programs. He is now head of the GNC (Guidance, Navigation and Control) department at ISL.

Michel Zasadzinski received the Ph.D. degree in automatic control from the Université de Lorraine, Nancy, France, in 1990. He has been an Assistant Professor at the Université de Lorraine and from 1992 to 2000, he has been a CNRS Researcher in the *Centre de Recherche en Automatique de Nancy* (CRAN, CNRS), Nancy, France. He is currently a Professor at the Institut Universitaire de Technologie (Longwy, Université de Lorraine), Lorraine, France. His research interests include the theory and application of robust control and filtering for linear and nonlinear systems, and for stochastic differential equations.

Mohamed Boutayeb received the Electrical Engineer degree from the *Ecole Hassania des Travaux Publics*, Casablanca, Morocco, in 1988 and the Ph.D. and H.D.R. degrees in automatic control from the University of Lorraine, Lorraine, France, in 1992 and 2000, respectively. From 1996 to 1997, he was an Invited Researcher at the Alexander von Humboldt Foundation, Germany. From 1997 to 1999, he was a Researcher at the *Centre National de la Recherche Scientifique* (CNRS), France. Since 2002, he has been a Full Professor at the University of Strasbourg, Strasbourg, France, and the University of Lorraine, respectively. His research interests include identification, state estimation, and control of dynamical systems. He is author and co-author of more than 200 publications in international journals and conferences.